



Fabrication, Characterization, and Modeling of Monolayer Molybdenum Disulfide Radio Frequency Transistors

by Alexander L Mazzoni, Matthew L Chin, Pankaj B Shah, Khamsouk Kingkeo, Madan Dubey, and Robert A Burke

Approved for public release; distribution is unlimited.

NOTICES

Disclaimers

The findings in this report are not to be construed as an official Department of the Army position unless so designated by other authorized documents.

Citation of manufacturer's or trade names does not constitute an official endorsement or approval of the use thereof.

Destroy this report when it is no longer needed. Do not return it to the originator.



Fabrication, Characterization, and Modeling of Monolayer Molybdenum Disulfide Radio Frequency Transistors

Alexander L Mazzoni

Oak Ridge Associated Universities (ORAU) Maryland

Robert A Burke
General Technical Services, LLC

Pankaj B Shah, Khamsouk Kingkeo, Matthew L Chin, and Madan Dubey

Sensors and Electron Devices Directorate, DEVCOM Army Research Laboratory

REPORT DOCUMENTATION PAGE

Form Approved OMB No. 0704-0188

Public reporting burden for this collection of information is estimated to average 1 hour per response, including the time for reviewing instructions, searching existing data sources, gathering and maintaining the data needed, and completing and reviewing the collection information. Send comments regarding this burden estimate or any other aspect of this collection of information, including suggestions for reducing the burden, to Department of Defense, Washington Headquarters Services, Directorate for Information Operations and Reports (0704-0188), 1215 Jefferson Davis Highway, Suite 1204, Arlington, VA 22202-4302. Respondents should be aware that notwithstanding any other provision of law, no person shall be subject to any penalty for failing to comply with a collection of information if it does not display a currently valid OMB control number.

PLEASE DO NOT RETURN YOUR FORM TO THE ABOVE ADDRESS.

1. REPORT DATE (DD-MM-YYYY)	2. REPORT TYPE	3. DATES COVERED (From - To)	
February 2021	Technical Report	January 2016–September 2017	
4. TITLE AND SUBTITLE		5a. CONTRACT NUMBER	
Fabrication, Characterization,	and Modeling of Monolayer Molybdenum		
Disulfide Radio Frequency Tra	ansistors	5b. GRANT NUMBER	
		5c. PROGRAM ELEMENT NUMBER	
C AUTHOR(C)		Ed project humaner	
6. AUTHOR(S)	y I Chin Dankai D Shah Vhamaayk Vingkaa	5d. PROJECT NUMBER	
Alexander L Mazzoni, Matthew L Chin, Pankaj B Shah, Khamsouk Kingkeo, Madan Dubey, and Robert A Burke			
		5e. TASK NUMBER	
		5f. WORK UNIT NUMBER	
7. PERFORMING ORGANIZATION NAI	WE(S) AND ADDRESS(ES)	8. PERFORMING ORGANIZATION REPORT NUMBER	
DEVCOM Army Research La	` ' '		
ATTN: FCDD-RLS-EM		ARL-TR-9141	
Aberdeen Proving Ground, MD 21005			
9. SPONSORING/MONITORING AGENCY NAME(S) AND ADDRESS(ES)		10. SPONSOR/MONITOR'S ACRONYM(S)	
		11. SPONSOR/MONITOR'S REPORT NUMBER(S)	
		11.3. Sussing Montroll's Report Holdberg)	

12. DISTRIBUTION/AVAILABILITY STATEMENT

Approved for public release; distribution is unlimited.

13. SUPPLEMENTARY NOTES

ORCID IDs: Alex Mazzoni, 0000-0002-8184-4373; Robert Burke, 0000-0002-1772-9848; Pankaj Shah, 0000-0003-2356-5664

14. ABSTRACT

Radio frequency (RF) transistors using US Army Combat Capabilities Development Command Army Research Laboratory—grown monolayer molybdenum disulfide (MoS_2) were fabricated and tested in the ground-signal-ground configuration. Devices were fabricated and characterized on both hard (silicon dioxide) and flexible (polyimide) substrates. Devices operated with de-embedded f_T and f_{max} over 3 GHz on rigid substrates and 1 GHz on flexible substrates. Standard metal—oxide—semiconductor field-effect transistor current-voltage equations are applied to experimental results of a DEVCOM Army Research Laboratory—fabricated RF transistors that use monolayer MoS_2 as the channel material. A method to accurately extract the key device parameters of threshold voltage, contact resistance, and transconductance is introduced and discussed. The experimental transistor curves deviate from the transistor models in regions of operation with both a high gate and drain bias. According to related literature, significant device self-heating occurs at these operation regimes causing significant velocity saturation/mobility degradation.

15. SUBJECT TERMS

2-D materials, van der Waals monolayers, radio frequency electronics, metal-oxide-semiconductor field-effect transistor, molybdenum disulfide

16. SECURITY CLASSIFICATION OF:		17. LIMITATION OF	18. NUMBER OF	19a. NAME OF RESPONSIBLE PERSON Alex Mazzoni	
a. REPORT	b. ABSTRACT	c. THIS PAGE	ABSTRACT	PAGES	19b. TELEPHONE NUMBER (Include area code)
Unclassified	Unclassified	Unclassified	UU	51	(301) 394-0494

Contents

List	of Fig	gures		v
List	of Ta	bles		vi
1.	Intr	oductio	on	1
2.	Me	thods		2
	2.1	MoS ₂ (Growth Process	2
	2.2	Device	Substrates	3
	2.3	MoS ₂ 7	Fransfer Process	4
	2.4	MoS ₂ F	RF FET Fabrication Process	5
		2.4.1	MoS ₂ Channel Etch	7
		2.4.2	Source and Drain Contact Metallization	10
		2.4.3	Top-Gate Dielectric Deposition	12
		2.4.4	Top-Gate Metallization	12
		2.4.5	Polyimide-Specific Fabrication Techniques	13
	2.5	DC Ele	ctrical Characterization	14
		2.5.1	Back-Gated Measurements	15
		2.5.2	Top-Gated Measurements	15
	2.6	RF Elec	ctrical Characterization	15
3.	Res	ults		16
	3.1	DC Ele	ctrical Data	16
		3.1.1	Back-Gated Testing	16
		3.1.2	Top-Gated Testing	18
	3.2	RF Elec	ctrical Data	20
		3.2.1	RF Performance on Rigid (SiO₂) Substrate	21
		3.2.2	RF Performance on Flexible (Polyimide) Substrate	22
		3.2.3	Comparison to Monolayer RF FET Performance in Literature	23
		3.2.4	RF Performance Comparison to Theoretical Limits	24
	3.3	Device	e I-V Modeling	24

	3.3.1	Simple FET Model with Contact Resistance	24
	3.3.2	FET Model Parameter Extraction	26
	3.3.3	Parameter Validation and Low-Field Mobility Calculation	28
	3.3.4	FET Model Inaccuracies at High Gate and Drain Fields	32
4.	Conclusions	S	37
5.	References		38
List	of Symbols,	Abbreviations, and Acronyms	41
Dist	ribution List		43

List of Figures

Fig. 1	Diagram of the MoS ₂ growth setup. The MoO ₃ powder and the substrates were loaded in the same alumina boat. The samples were placed face down on top of the alumina boat and the MoO ₃ powder was spread along the base of the boat.	3
Fig. 2	Cross-section of the device substrate prior to MoS ₂ transfer. The highly doped Si wafer acted as a back-gate contact for the 300-nm SiO ₂ dielectric, but the polyimide film is too thick to be operated in a back-gated configuration.	4
Fig. 3	Cross-section of the device stack after MoS ₂ transfer	5
Fig. 4	Optical image of a completed device (left) and corresponding cross- section (right); red line on optical image indicating location of cross- section	6
Fig. 5	CAD drawing of the RF transistor fabricated with important dimensions labeled. The colors correspond to the different layers: green = MoS ₂ channel, magenta = drain and source metal contact layer, and cyan = top-gate metal layer.	7
Fig. 6	Optical image of a device after EBL exposure and development to form the MoS ₂ channel, but before MoS ₂ etching	8
Fig. 7	Channel area after the channel-defining RIE, but before PMMA removal in acetone	9
Fig. 8	Channel area after RIE and PMMA removal in acetone	0
Fig. 9	Device after metal contact EBL, prior to metal evaporation for the source/drain contacts	1
Fig. 10	Device after source/drain metal contact deposition and liftoff 1	2
Fig. 11	Device after top-gate metal contact deposition and liftoff 1	3
Fig. 12	Completed RF FET on polyimide1	4
Fig. 13	CAD for the short and open test structures fabricated for de- embedding	6
Fig. 14	Back-gated I_{DS} vs. V_{GS} example measurement, $V_{DS} = 100$ mV	7
Fig. 15	Mobility extracted from the back-gated I_{DS} vs. V_{GS} example measurement	8
Fig. 16	Top-gated I_{DS} vs. V_{GS} example measurement	9
Fig. 17	Top-gated I_{DS} vs. V_{DS} example measurement	0
Fig. 18	Rigid substrate: $f_T \sim 180 \text{ MHz/}3.3 \text{ GHz (extrinsic/intrinsic)}2$	1
Fig. 19	Rigid substrate: $f_{max} \sim 2.4$ GHz/3.5 GHz (extrinsic/intrinsic)	2
Fig. 20	Polyimide substrate: $f_T \sim 300 \text{ MHz/1 GHz}$ (extrinsic/intrinsic)	2
Fig. 21	Polyimide substrate: $f_{max} \sim 1.1$ GHz/1.1 GHz (extrinsic/intrinsic) 2	3

Table 1	Summary of intrinsic RF device performance 23
List of 1	Tables Tables
	extracted values X1, X2, and X3. Subthreshold current modeling was ignored for simplicity; this explains the low current computed for V_{GS} < -10 V
Fig. 34	Experimental results vs. computed I_{DS} – V_{DD} curves plotted using
Fig. 33	Experimental results vs. computed $I_{DS-}V_{DD}$ curves plotted using extracted values X1, X2, and X3
Fig. 32	$I_{DS-}V_{DD}$ curves plotted using extracted values X1, X2, and X3 35
Fig. 31	Calculated voltage drops due to contact resistance, X1. The specific contact resistance of this device was $2.56~\mathrm{k}\Omega\cdot\mu\mathrm{m}$
Fig. 30	$I_{DS-}V_{DS}$ curves plotted using extracted values X2 and X3
Fig. 29	Field-effect mobility extracted from the RF FET $I_{DS-}V_{GS}$ curve after incorporating the voltage dropped across the contact resistance 32
Fig. 28	Field-effect mobility extracted from the RF FET $I_{DS-}V_{GS}$ curve as measured (not considering contact resistance)
Fig. 27	After extracting the contact resistance, we can determine how much of the applied voltage V_{DD} is dropped across the channel vs. the contact resistance. At low gate voltages most of the voltage drops across the channel, but at high gate voltages most drops across the contact resistance.
Fig. 26	RF FET $I_{DS-}V_{GS}$ curve (notice the extracted threshold voltage of -10.45 from the $I_{DS-}V_{DS}$ curves qualitatively makes sense)
Fig. 25	Extrapolation of the total resistance to higher gate voltages, showing the limit of twice the contact resistance as the dashed horizontal line and threshold voltage as the vertical line28
Fig. 24	Total resistance: experimental values compared to the model 27
Fig. 23	$I_{DS-}V_{DS}$ curve of an RF FET on the rigid substrate. Dashed green box indicates region used to fit FET parameters
Fig. 22	Simple transistor model including contact resistances

1. Introduction

In 2004, researchers established the ability to create a 2-D sheet of material only a single-atom thick with the demonstration of graphene, a monolayer of carbon atoms exfoliated from the bulk and layered material graphite. This method to produce 2-D monolayers was then quickly applied to other common layered materials, including molybdenum disulfide (MoS₂). Although back-gated field-effect transistors (FETs) using monolayer MoS₂ as the semiconducting channel were demonstrated in 2005, the carrier mobility measured many orders of magnitude lower than the mobility in graphene, and research into the electronic properties of 2-D materials focused mainly on graphene. A few factors renewed interest in the electronic properties of MoS₂ in the early 2010s such as the limitations realized in graphene electronics from its lack of a bandgap, the observation of an indirect-to-direct bandgap transition when MoS₂ is thinned to a monolayer, ^{3,4} the demonstration of improved monolayer MoS₂ transistor performance, ^{5,6} and the ability to grow large-area MoS₂ via a chemical vapor deposition (CVD) method. The single stability to grow large-area MoS₂ via a chemical vapor deposition (CVD) method.

The emphasis on research and development of MoS_2 transistors occurred after that of graphene transistors, and that research is often referenced for guidance or comparison. In terms of transistors for RF applications, the high carrier mobility and velocity in graphene excited researchers for the potential of pushing the limits on transistor operating speed. Graphene FETs quickly demonstrated competitive performance with state-of-the-art III-V and silicon (Si) transistors in terms of cutoff frequency, f_T . However, the lack of a bandgap in graphene prevents the normal transistor saturation needed to have a high output resistance and graphene transistors could not compete in terms of power gain or the maximum frequency of operation metric, f_{max} .

In a similar manner, although MoS₂ has a bandgap and shows clear saturating behavior, its carrier mobility is lower and could not compete in either RF performance metric.⁹

Due to the inability of 2-D materials to immediately compete with state-of-the-art devices in traditional digital or RF applications, researchers started looking for niche applications that take advantage of 2-D materials' thinness and the unique deposition methods like inkjet printing or fabrication processes like the polymer-assisted transfer method. Around 2015, one such application space popularly explored was using 2-D materials such as MoS₂ as candidates for flexible RF electronics due to their high elastic strain limit¹⁰ and ability to transfer to arbitrary surfaces. In this area of flexible or transparent electronics, suggested at least as

early as 2006–2007 as a target area for MoS₂ electronics, ¹¹ transistors made from 2-D materials are often compared in performance to organic semiconductors.

This report documents the work to achieve the following goals derived from the Biennial Program Plan¹² of:

- 1) Monolayer MoS₂ FETs operating in the GHz frequencies (2016)
- 2) Monolayer MoS₂ FETs operating above a GHz on flexible substrates (2017)

Efforts to fabricate transistors out of monolayer MoS₂ using an entirely in-house operation to grow the material, make the device, and test the device are detailed in this report. The performance of the device is then compared to standard transistor models, other monolayer MoS₂ RF FET performance published in literature, ^{13,14} and to the theoretical maximum performance of phonon-limited transport. ^{15,16}

2. Methods

The following steps are covered in detail in this section:

- 1) MoS_2 growth process
- 2) Preparation of the device substrates (rigid and flexible)
- 3) Process used to physically transfer MoS₂ from the growth substrate to the device substrate
- 4) Fabrication of RF FETs after material transfer
- 5) DC testing of the MoS₂ FETs
- 6) RF testing of the MoS₂ FETs

2.1 MoS₂ Growth Process

MoS₂ was grown on 15- \times 16-mm thermal oxide (220 nm) chips in a tube furnace via powder vaporization using sulfur and molybdenum trioxide (MoO₃) powder precursors. The growth was performed in a tube furnace with heating tape upstream of the hot zone (Fig. 1). Sulfur powder was located upstream, outside of the furnace heating zone to limit the sulfur vapor pressure, and was instead controlled by the heating tape. Alumina boats were used for holding the MoO₃ powder, sulfur powder, and the substrates for growth. Argon was used as a carrier gas for the growth process. The heating tape was set to 275 °C, while the furnace temperature was set to 650 °C. Before growth, 40 μ L of perylene-3,4,9,10-tetracarboxylic acid tetrapotassium salt was spin-coated at 2000 rpm on the samples to improve seeding for the growth process.

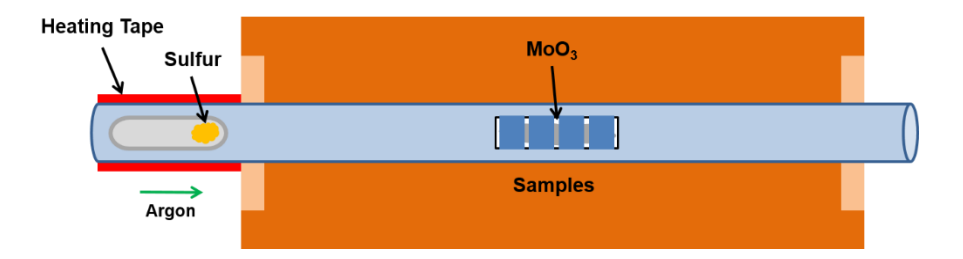


Fig. 1 Diagram of the MoS_2 growth setup. The MoO_3 powder and the substrates were loaded in the same alumina boat. The samples were placed face down on top of the alumina boat and the MoO_3 powder was spread along the base of the boat.

2.2 Device Substrates

The RF FETs were fabricated on top of two different substrates. The first was a standard thermal oxide chip (300 nm), the second was a layer of polyimide spun on a Si chip. In both cases, the MoS_2 layer was moved from the growth substrate (220-nm thermal oxide chip) to the device substrate via the transfer method described in Section 2.3.

A spin-on polyimide was chosen to enable standard fabrication on a rigid carrier wafer, with the ability to peel off the flexible device upon completion. The specific polymer chosen was HD Microsystems Polyimide PI 2611. This polyimide has an associated optional adhesion promoter, VM-651. The polyimide was spun onto a Si wafer at 2000 rpm for 60 s and then soft baked on a hot plate at 150 °C for 2 min. This was performed two times to create a thicker layer. To cure the polyimide, the wafer was loaded into a vacuum furnace (IVI Corp.) with controlled heat-ramping rates. The furnace ramped from room temperature to 250 °C over 1 h, stayed at temperature for 2 h, then took 1 h to cool down to room temperature. A slow ramping time for temperature heat-up and cool-down was critical to prevent any delamination. According to the data sheet, the polyimide thickness should be approximately 9 µm after curing.

A layer of aluminum oxide (Al₂O₃) was deposited on both substrates to serve as a common bottom interface of the MoS₂ transistor. First, a 1-nm Al seed layer was deposited via electron beam evaporation (CHA Industries) at a pressure of 10⁻⁶ Torr. After the Al seed-layer deposition, the sample sat out in the ambient cleanroom environment to oxidize. A total of 250 cycles of plasma-enhanced atomic layer deposition (PEALD) Al₂O₃ were then deposited (Kurt J. Lesker Company) at 200 °C using oxygen (O₂) and trimethylaluminum (TMA) precursors. This PEALD coating was deposited on both substrates to provide a similar interface with the MoS₂ layer, enabling a more direct comparison between the rigid (silicon dioxide [SiO₂]) and flexible (polyimide) substrate devices.

A cross-section of the device substrates prior to MoS₂ transfer is provided in Fig. 2.

PEALD Al₂O₃

SiO₂ (300 nm) or Polyimide Film

Si (p++)

Fig. 2 Cross-section of the device substrate prior to MoS_2 transfer. The highly doped Si wafer acted as a back-gate contact for the 300-nm SiO_2 dielectric, but the polyimide film is too thick to be operated in a back-gated configuration.

On top of this substrate stack, MoS_2 material was transferred (described in Section 2.3) and then underwent the RF FET fabrication process shown in Section 2.4.

2.3 MoS₂ Transfer Process

The transfer process used a polymethyl methacrylate (PMMA) spin-cast layer to protect the MoS_2 and potassium hydroxide (KOH) to separate the MoS_2 from the SiO_2 growth substrate. The specific details for the transfer process are as follows.

PMMA 950 A9 was spun onto the MoS₂/SiO₂/Si growth substrate stack at 2000 rpm for 60 s and then soft baked at 50 °C in air for 30 min. After air-drying in a fume hood for an additional 3 h at room temperature, the PMMA was scraped from the edges of the growth substrate with a razor blade.

A solution of 15% KOH by weight was prepared by dissolving KOH pellets in deionized (DI) water. The PMMA-coated MoS₂ substrate was floated on the KOH solution at room temperature and left in the solution until interfacial interactions between the MoS₂, SiO₂, and KOH solution caused the PMMA/MoS₂ layer to release from the SiO₂/Si substrate.

Upon release, the MoS₂ with the PMMA handling layer was transferred from the KOH solution into a DI water bath, where it was floated for 10 min to disperse any KOH residue still present on the MoS₂. This PMMA/MoS₂ film stack was transferred again to another DI water bath, where it sat for another 10 min to further dilute any KOH residue. Finally, the PMMA/MoS₂ film stack was transferred onto the target substrate within the DI water bath. Once the transfer was complete, the PMMA/MoS₂ film stack was lightly dried with nitrogen gas (N₂) to remove any

interfacial water. The sample was then dried at room temperature in a fume hood overnight.

After drying overnight, the PMMA layer was removed from the MoS_2 by immersing the sample in an acetone bath at room temperature for at least 2 h. Afterward, the sample was taken out of the acetone, rinsed with isopropyl alcohol (IPA), and dried using N_2 . Forming gas anneals can help remove any remaining PMMA residue, but for these devices a forming gas anneal was skipped to limit the exposure of the polyimide layer to high temperatures. At this point, the transferred MoS_2 film was ready for processing (Fig. 3).

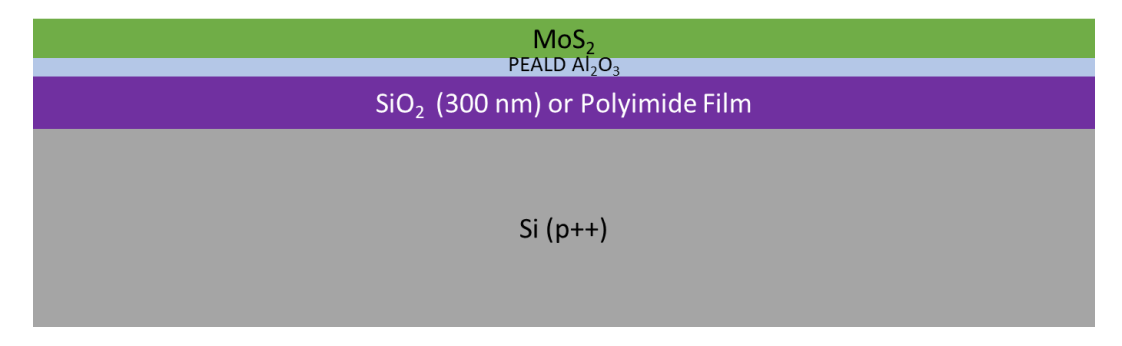


Fig. 3 Cross-section of the device stack after MoS₂ transfer

2.4 MoS₂ RF FET Fabrication Process

After material transfer, areas of clean, monolayer MoS₂ were identified via optical microscopy (Olympus OLS 4000 LEXT), and the following steps were performed:

- 1) MoS₂ channel etch
- 2) Source and drain contact metallization
- 3) Top-gate dielectric deposition
- 4) Top-gate contact metallization

All patterning for etching and deposition steps was performed using a PMMA layer defined by electron beam lithography (EBL). PMMA 950 A4 was spun at 2000 rpm, giving a thickness around 300 nm, and baked on a hotplate at 185 °C for 2 min. The base exposure dose used was 850 μ C/cm² and development was performed in a 10-mL methyl isobutyl ketone (MIBK): 25-mL IPA solution for 75 s, followed by N₂ drying.

A single RF FET device design was used and around 10 identical devices were fabricated on both substrate types. To understand the device fabricated, in Fig. 4 we first show an example optical image of a completed device on the thermal oxide substrate along with a simplified cross-section of the device.

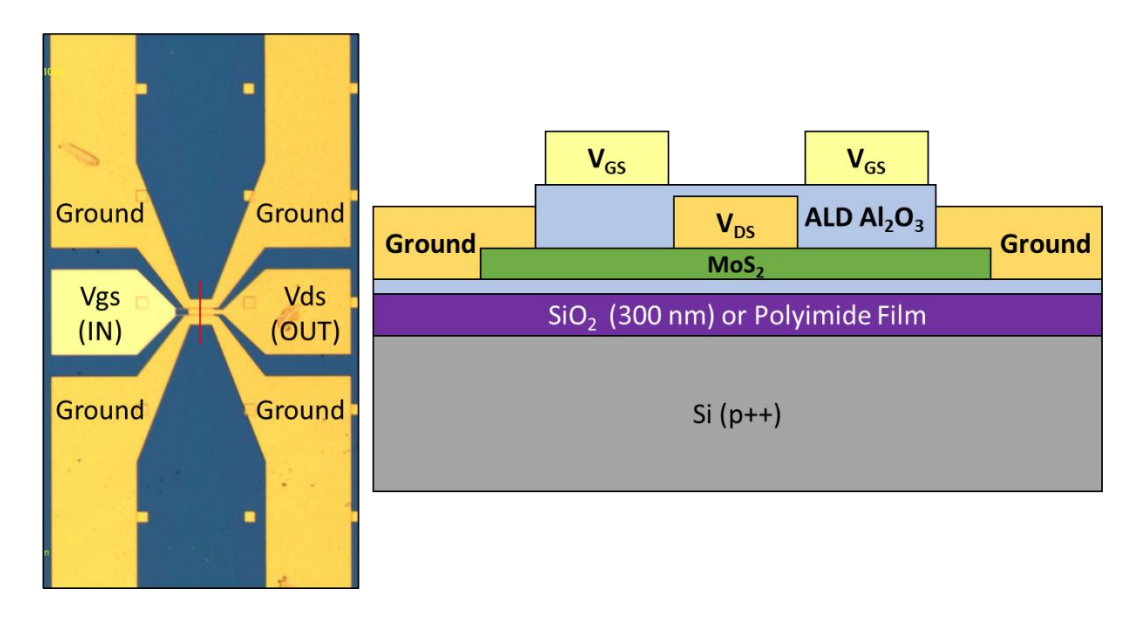


Fig. 4 Optical image of a completed device (left) and corresponding cross-section (right); red line on optical image indicating location of cross-section

The device was designed to be tested in the ground-signal-ground (GSG) configuration, accommodating probe pitches of $50{\text -}150\,\mu\text{m}$. A zoomed-in image of the RF FET computer-aided design (CAD) is provided in Fig. 5. The gate length was 400 nm and the drain-source distance was 600 nm, meaning there was a 100-nm gap on either side to allow for some alignment inaccuracy. The transistor channel width was $10\,\mu\text{m}$.

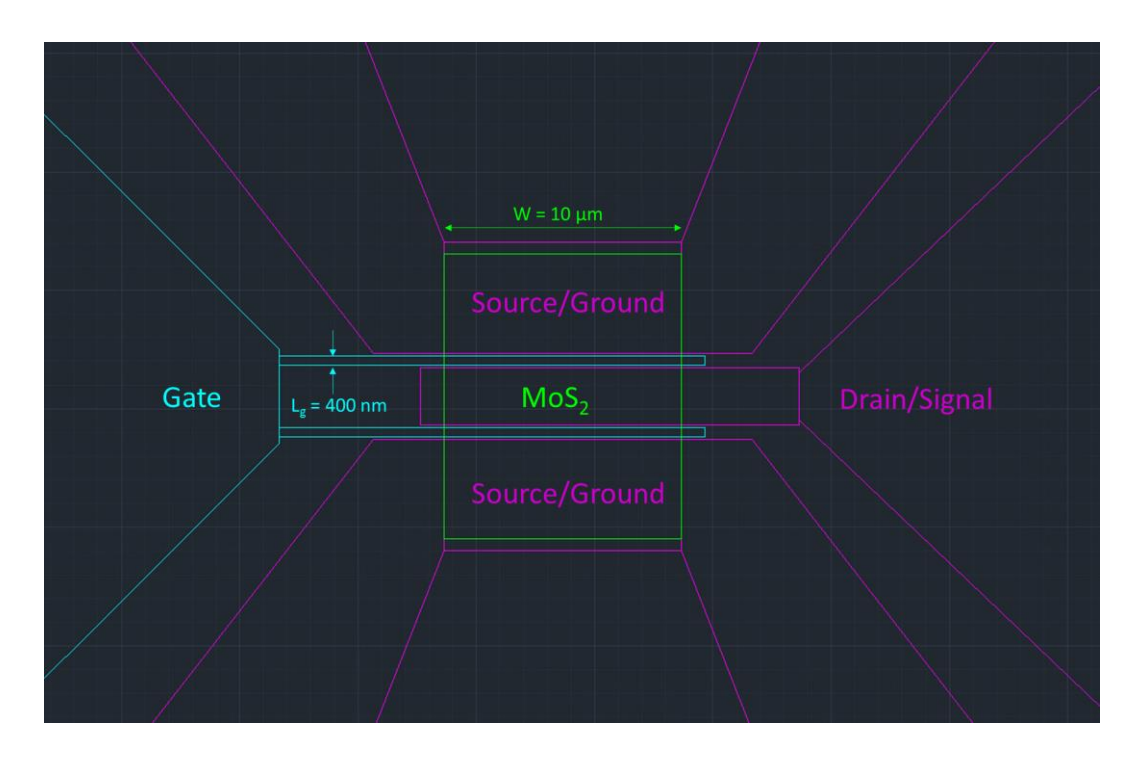


Fig. 5 CAD drawing of the RF transistor fabricated with important dimensions labeled. The colors correspond to the different layers: green = MoS_2 channel, magenta = drain and source metal contact layer, and cyan = top-gate metal layer.

2.4.1 MoS₂ Channel Etch

The MoS₂ channel (green section in Figs. 4 and 5) dimensions were formed through 45 s of reactive ion etching (RIE) using 15 sccm of tetrafluoromethane (CF₄), 5 sccm of O₂, and 200 W of RF power (Ulvac NE550e Etcher). It should be noted that since these devices were made, we have switched to a dry-etching process based on chlorine (Cl₂) and O₂, with a pure O₂ second step to minimize residue.¹⁷

Figure 6 shows an example device after the channel-defining EBL step, but before the RIE step. The example device shown is on the 300-nm thermal oxide wafer and as can be seen in the optical image, the MoS_2 growth was not uniform and did not cover the whole chip. The gray rectangle represents the area chosen for device fabrication and was protected by PMMA while the rest of the MoS_2 was removed. It should be noted that sometimes, as in this example device, the area of MoS_2 to be covered with metal contacts had small regions of bilayer growth, but the areas that form the transistor channel were always monolayer growth.

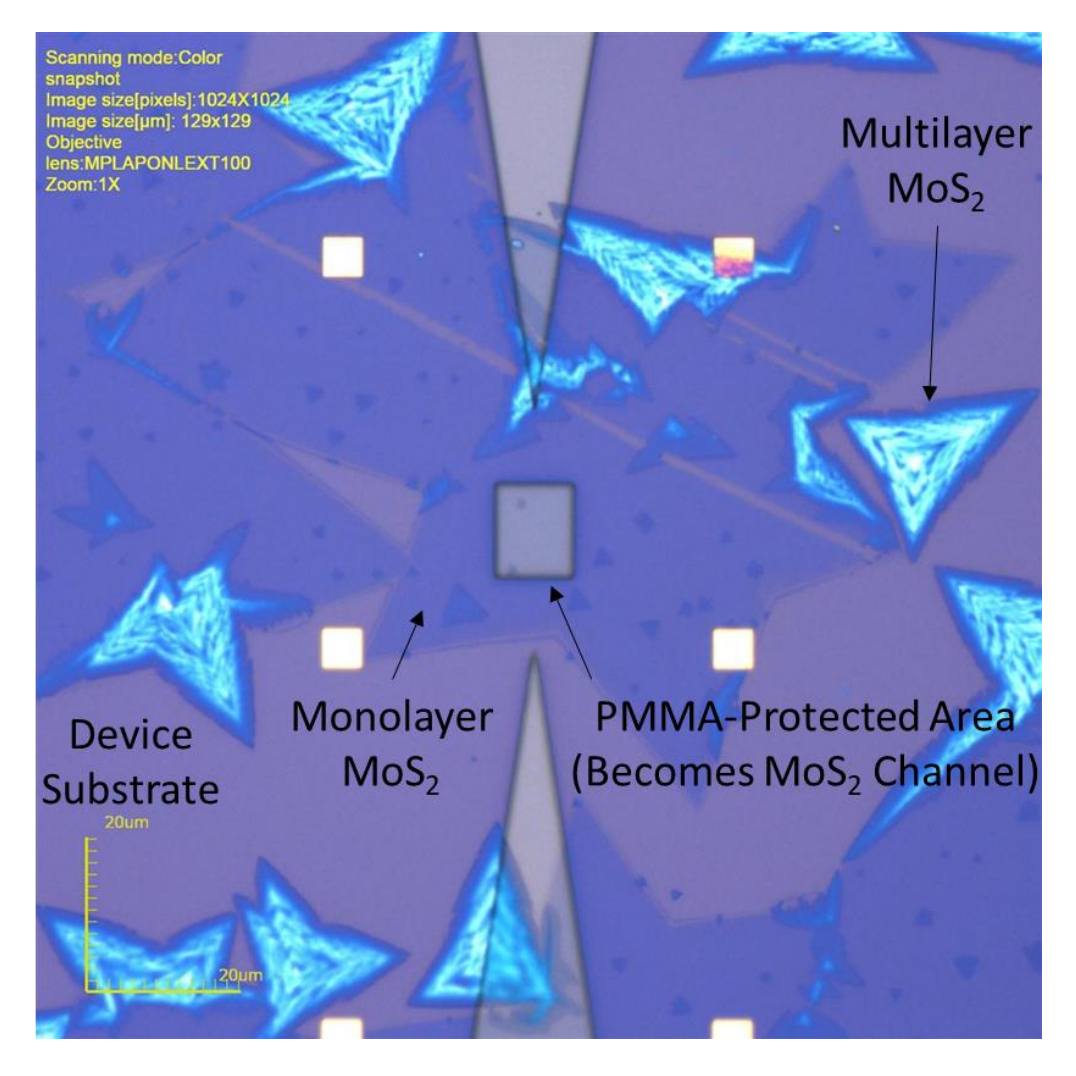


Fig. 6 Optical image of a device after EBL exposure and development to form the MoS₂ channel, but before MoS₂ etching

Figure 7 shows the same example device after the RIE step was performed to etch away all the MoS_2 , but prior to removal of the PMMA in acetone. Although it is not shown in the image, the boundary of where we performed the RIE step extended past where the metal contact pads will be by around 10 μ m in all directions to avoid unwanted conduction pathways across the MoS_2 growth or between devices.



Fig. 7 Channel area after the channel-defining RIE, but before PMMA removal in acetone Lastly, Fig. 8 shows the MoS_2 channel after removal of the PMMA layer in acetone.

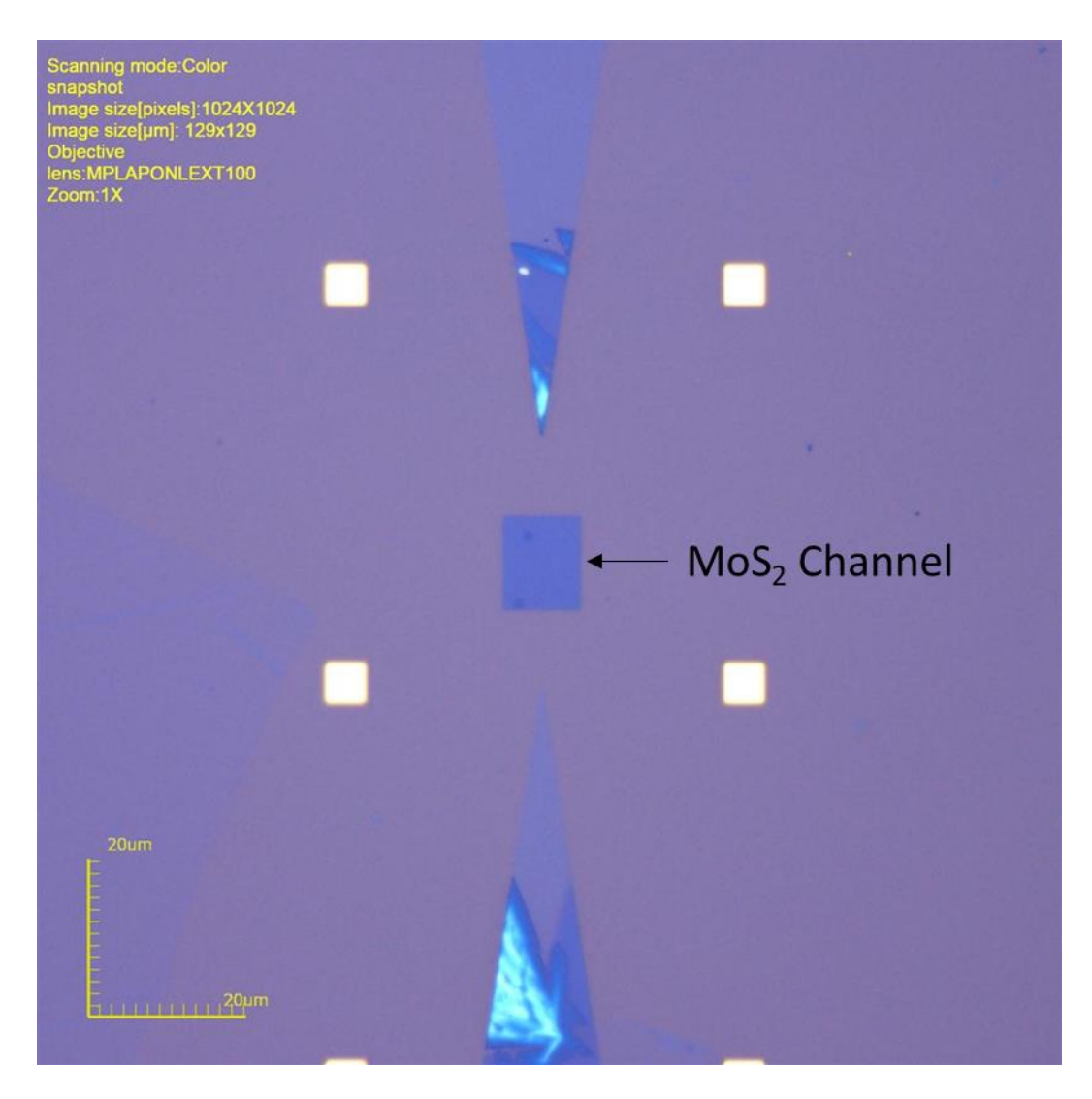
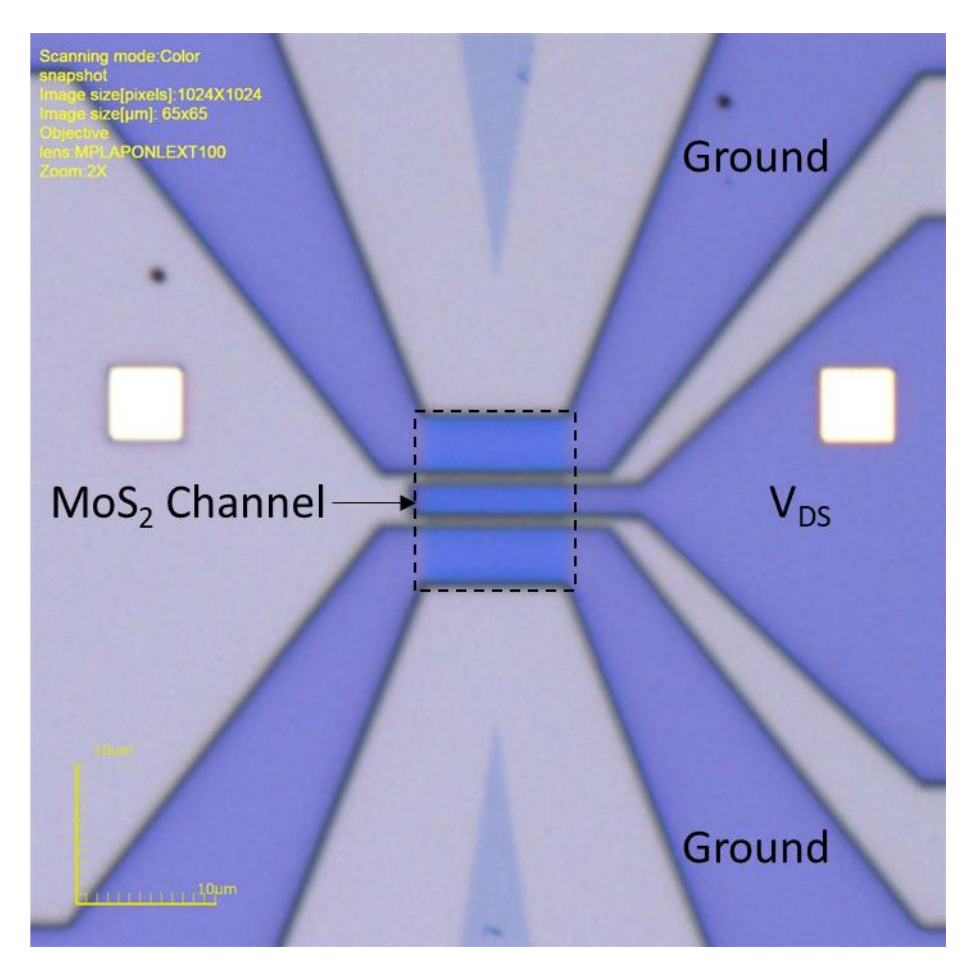


Fig. 8 Channel area after RIE and PMMA removal in acetone

2.4.2 Source and Drain Contact Metallization

Metal source/drain contacts (darker-gold layer in Fig. 4, magenta in Fig. 5) of silver (Ag)/gold (Au) (30/70 nm) were deposited via electron beam evaporation (CHA Industries) at a pressure of 1×10^{-6} Torr, followed by liftoff in acetone.

Figure 9 shows an example device after the source/drain contact EBL step, but before the metallization step. The MoS_2 channel formed by the previous RIE step is indicated by the dashed rectangle and the electrical nodes to be formed are labeled accordingly with Figs. 4 and 5.



 $\label{eq:fig.9} \textbf{Device after metal contact EBL, prior to metal evaporation for the source/drain contacts}$

After the metal contact layer was deposited, the chips were soaked in acetone for liftoff. The acetone was not heated above $40\,^{\circ}\mathrm{C}$ to avoid bubbling that can lead to delamination of the polyimide layer. Figure $10\,\mathrm{shows}$ an example device after metal deposition and liftoff.

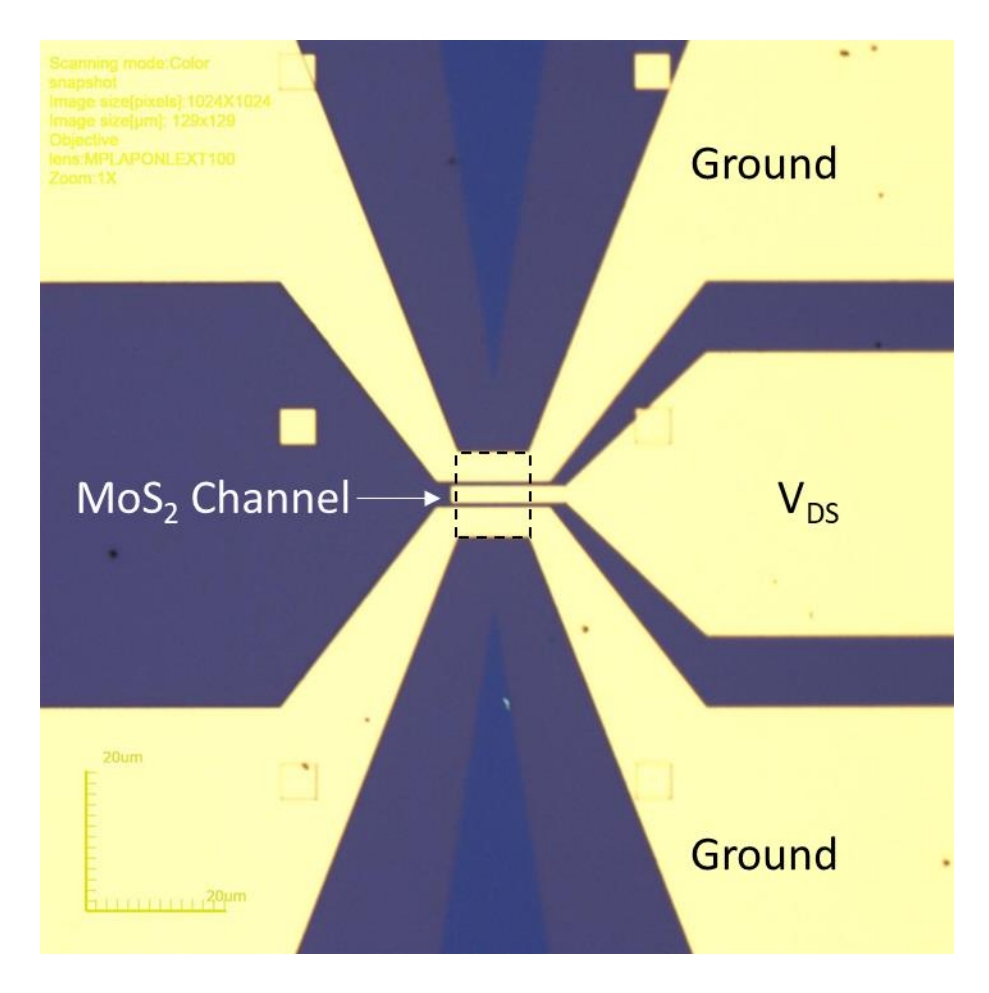


Fig. 10 Device after source/drain metal contact deposition and liftoff

2.4.3 Top-Gate Dielectric Deposition

The top-gate dielectric deposition process was identical to the process used for the bottom dielectric interface described in Section 2.2. Once again, a 1-nm Al seed layer was deposited via e-beam evaporation, allowed to oxidize in air, then 250 cycles of Al₂O₃ were deposited via PEALD using O₂ and TMA precursors.

2.4.4 Top-Gate Metallization

The final step in the fabrication process was the deposition of the top-gate metal. This process was identical to the source/drain contact metallization, except the metals deposited were nickel (Ni)/Au (20/80 nm) (Fig. 11).

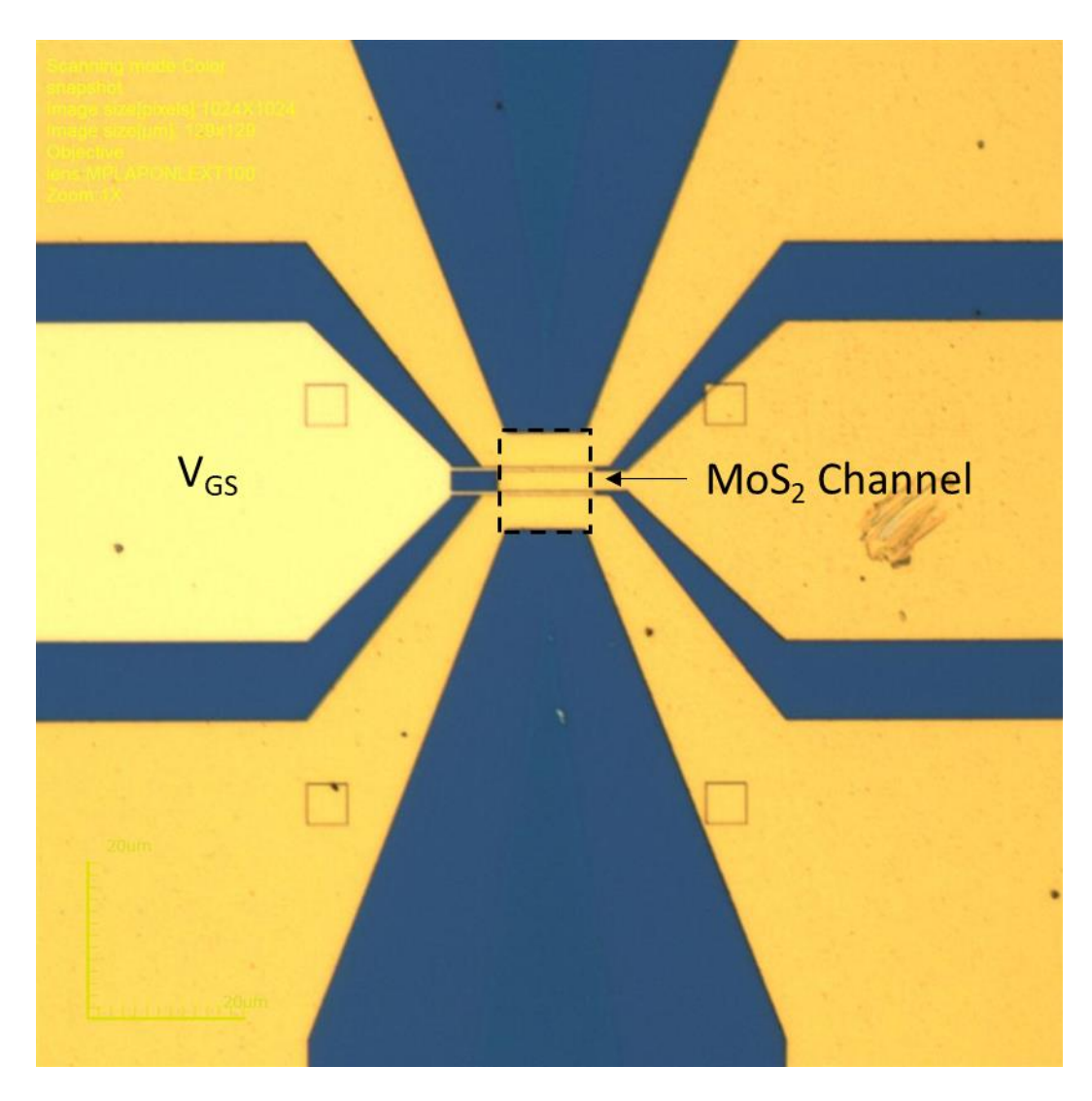


Fig. 11 Device after top-gate metal contact deposition and liftoff

We experimented with adding a top-dielectric etch step to get clean access to the metal contact pads but determined that the probes easily scratched through the PEALD layer and had reliable electrical contact.

2.4.5 Polyimide-Specific Fabrication Techniques

We were apprehensive about performing EBL on a nonconductive surface (polyimide), so we used a conductive layer of poly(3,4-ethylenedioxythiophene)-poly(styrenesulfonate) (PEDOT:PSS), 3% to 4% Sigma Aldrich 655201 to avoid charging artifacts. Sometimes PEDOT:PSS can be difficult to remove after exposing large areas to high-energy electrons. To achieve full removal of the PEDOT:PSS film, the samples were soaked in 80 °C water and lightly agitated until the film lifted off (usually within a minute or two). After removal of the conductive

film, the PMMA was developed as usual in the MIBK and IPA solution. Figure 12 shows an optical image of a completed RF FET on the polyimide substrate.

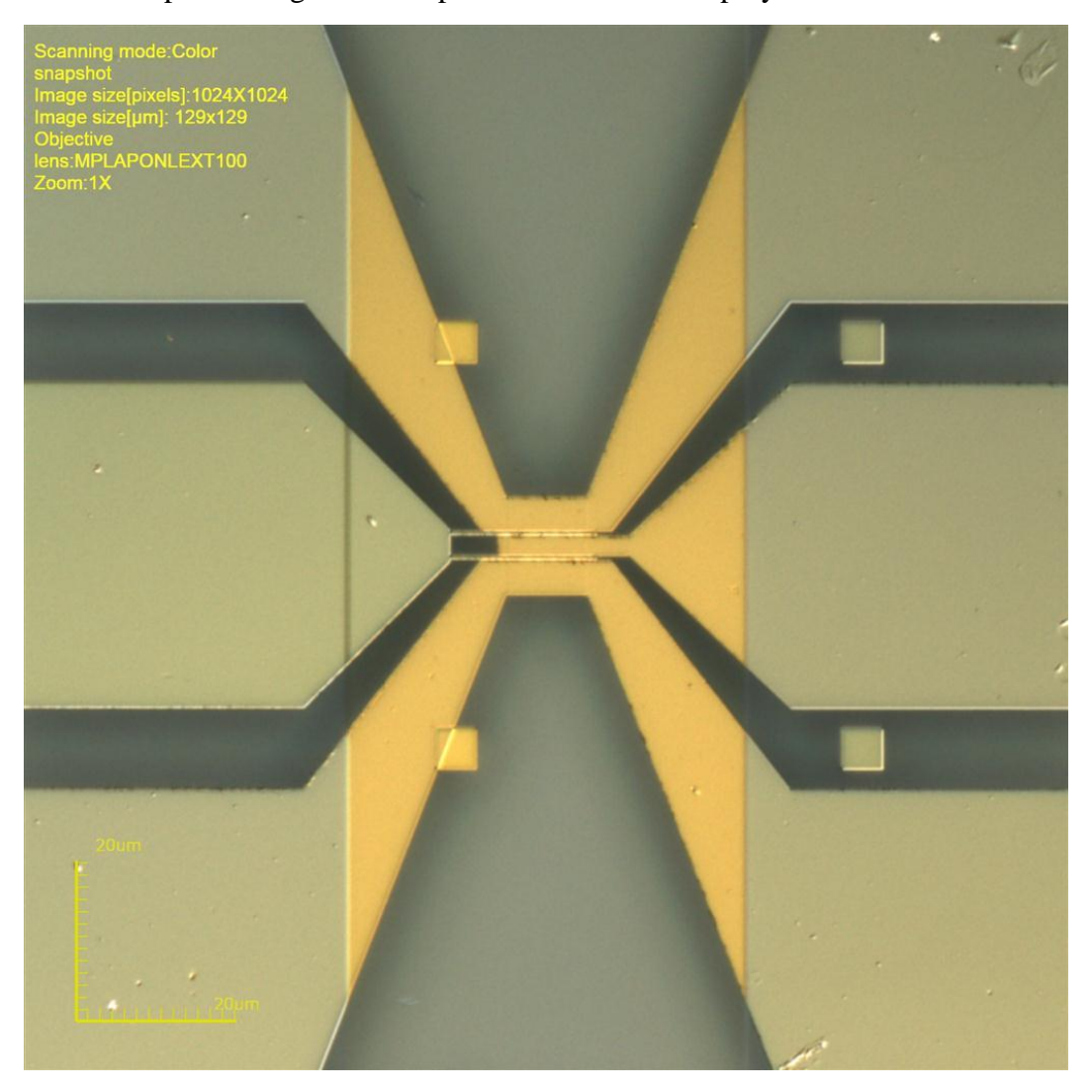


Fig. 12 Completed RF FET on polyimide

2.5 DC Electrical Characterization

All devices were tested at room temperature in a vacuum probe station at a pressure no higher than 5×10^{-5} Torr. Prior to testing, the devices were annealed overnight at 400 °K in vacuum to drive out water vapor. A Keithley 4200 Semiconductor Characterization System was used to perform the electrical measurements. The viewport was covered with Al foil to block any light from entering the probe station.

2.5.1 Back-Gated Measurements

After the source/drain contact metallization step, devices without the polyimide layer were tested to get a baseline measurement using the doped Si substrate as a back-gate electrode. Since the polyimide substrate is insulating, those devices could only be measured after completing the entire top-gate fabrication process.

Devices were tested with a constant drain-source bias (V_{DS}) of 100 mV, while sweeping the back-gate voltage (V_{GS}) back and forth from -30 to +60 V and measuring the drain-source current (I_{DS}) .

Calculations in this report for back-gated measurements used a relative permittivity of $\varepsilon_{ox} = 3.9$ for SiO₂ and a thickness of $t_{ox} = 300$ nm.

2.5.2 Top-Gated Measurements

After finishing the fabrication process, devices were tested to determine proper DC biasing conditions for the RF testing. Devices were tested with a constant V_{DS} of 100 mV, while sweeping the top-gate voltage back and forth from -10 to +10 V (or sometimes -20 to +10 V when looking for complete turnoff, usually avoided to limit the electric field across the gate oxide).

From the $I_{DS-}V_{GS}$ measurement, a range of suitable top-gate voltages were chosen to step through, while V_{DS} was swept from 0 to 5 V. These $I_{DS-}V_{DS}$ curves provide the information for determining DC biasing conditions during the RF testing.

The calculations in this report for top-gated measurements used a relative permittivity of $\varepsilon_{ox} = 9$ for Al₂O₃ and a thickness of $t_{ox} = 25$ nm.

2.6 RF Electrical Characterization

The devices with the highest transconductance and current saturation were chosen for RF testing. RF measurements were made on a Cascade Summit Probe station using a Keysight PNA-X network analyzer to obtain the small-signal S-parameter data up to 30 GHz. Being small signal, we verified that the RF power was kept quite low to avoid nonlinear effects during the measurements, while also minimizing noise effects. DC bias was provided by a Keysight B1500 parametric analyzer. GGB Industries' GSG coplanar RF probes were used to apply the DC bias and launch the RF signal into the FET. During fabrication mask layout, we verified that a 50-ohm environment existed at the probe pads and through the transition structure to the transistor using the software Keysight ADS Momentum. While RF testing, short-open-load-thru calibration was used to calibrate up to the probe tips, followed by an open-short de-embedding¹⁸ to remove the parasitic effects of the large pads use for landing the probes (Fig. 13). Analysis of the RF data was performed using Keysight ADS software.

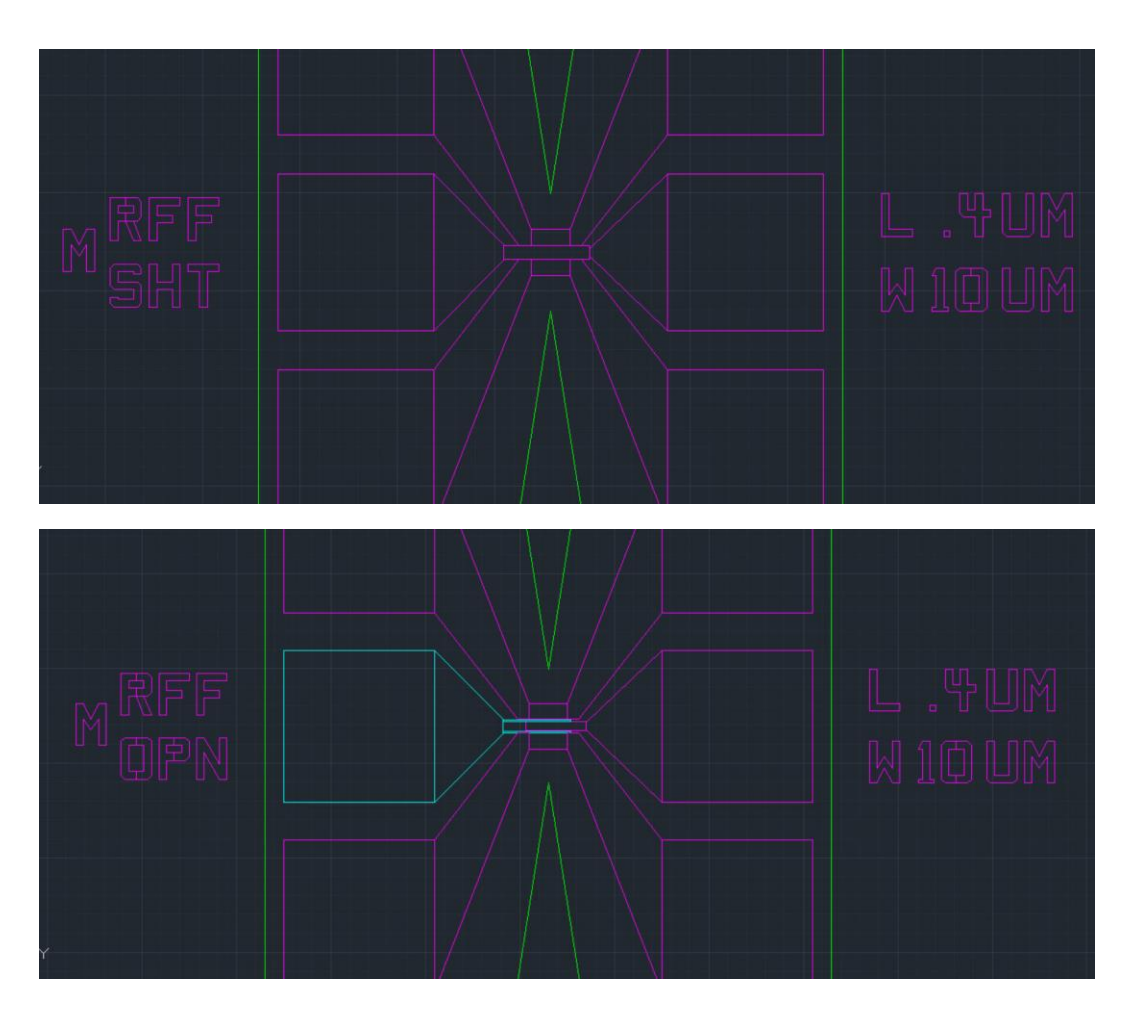


Fig. 13 CAD for the short and open test structures fabricated for de-embedding

3. Results

Section 3.1 provides example current-voltage (I-V) curves from the DC electrical testing.

Section 3.2 compiles the RF performance achieved and compares it to similar devices in the literature and the theoretical limits.

Section 3.3 compares the top-gated transistor I-V curves to standard transistor models and provides a potential explanation for the deviation in behavior.

3.1 DC Electrical Data

3.1.1 Back-Gated Testing

A typical transfer curve obtained from the back-gated testing is shown in Fig. 14. The transistors were completely off at a V_{GS} of -30 V and had an I_{ON}/I_{OFF}

approximately 10^7 – 10^8 , though this is determined primarily by the capability to accurately measure the off-current.

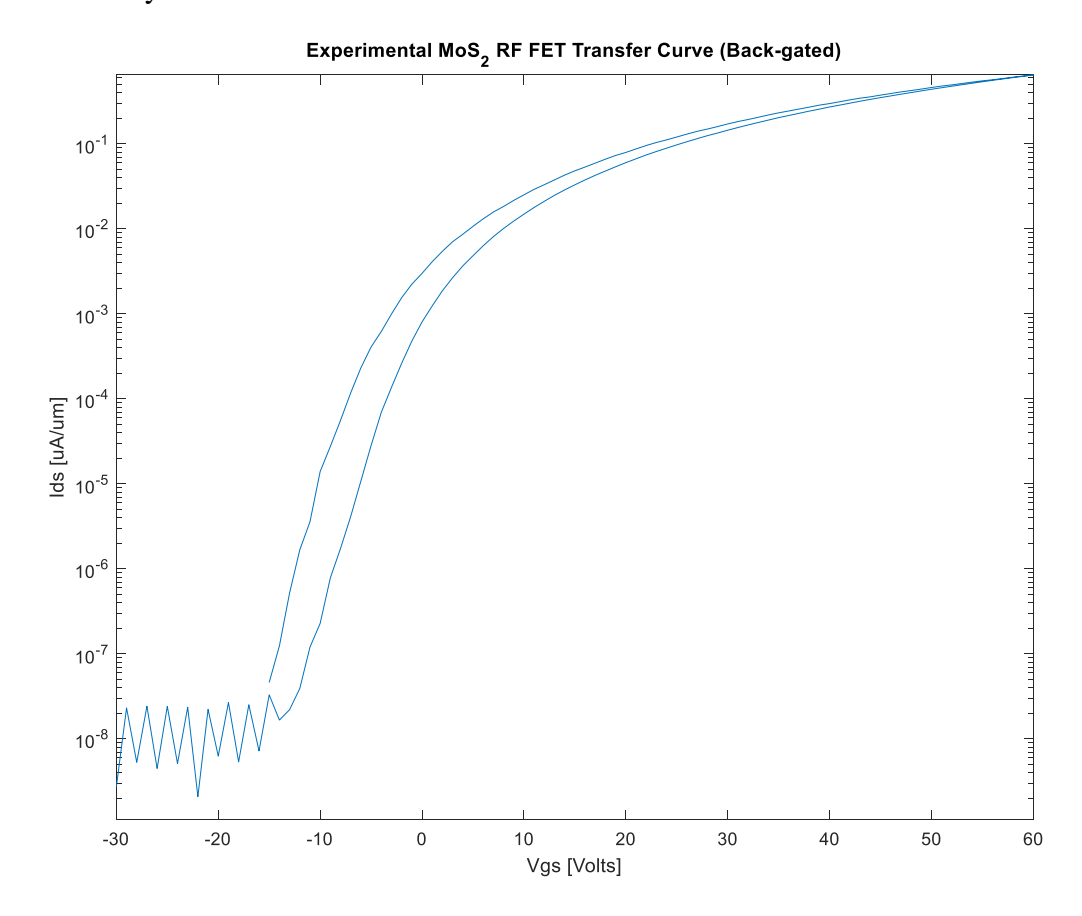


Fig. 14 Back-gated I_{DS} vs. V_{GS} example measurement, $V_{DS} = 100 \text{ mV}$

Field-effect mobility was determined from the $I_{DS-}V_{GS}$ characteristics (Fig. 15) via Eq. 1:

$$\mu_{FE} = \frac{d_{V_{DS}}^{I_{DS}}}{dV_{GS}} \times \frac{1}{c_{ox}} \times \frac{L}{W}, \qquad (1)$$

where V_{DS} is the applied drain-source voltage, I_{DS} is the measured drain current, V_{GS} is the applied gate-source voltage, L/W is the ratio of channel dimensions, and C_{ox} is the gate-channel capacitance per unit area:

$$C_{ox} = \frac{\varepsilon_{ox}\varepsilon_0}{t_{ox}},\tag{2}$$

where ε_{ox} is the relative permittivity of the gate dielectric, ε_0 is the permittivity of free space, and t_{ox} is the gate dielectric thickness.

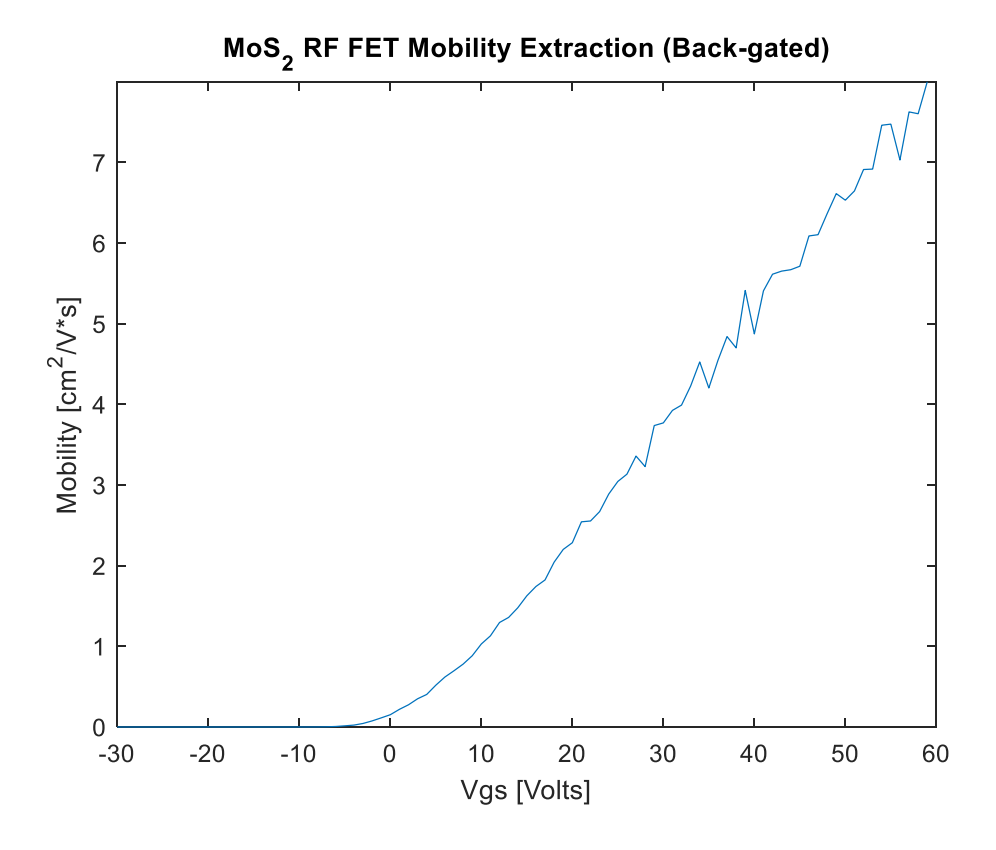


Fig. 15 Mobility extracted from the back-gated I_{DS} vs. V_{GS} example measurement

This version of mobility extraction is based off a two-point probe measurement, meaning that the actual intrinsic mobility of the material is higher since contact resistance is not considered. This transfer curve and carrier mobility is consistent with devices we have measured previously using monolayer MoS₂ grown in a similar manner.¹⁹

3.1.2 Top-Gated Testing

A typical transfer curve obtained from the top-gated testing is shown in Fig. 16. The top-gate fabrication process shifted the threshold voltage, causing the devices to be on at 0 gate voltage. This threshold voltage shift is consistent with results in the literature and other devices fabricated at the US Army Combat Capabilities Development Command Army Research Laboratory.^{20,21}

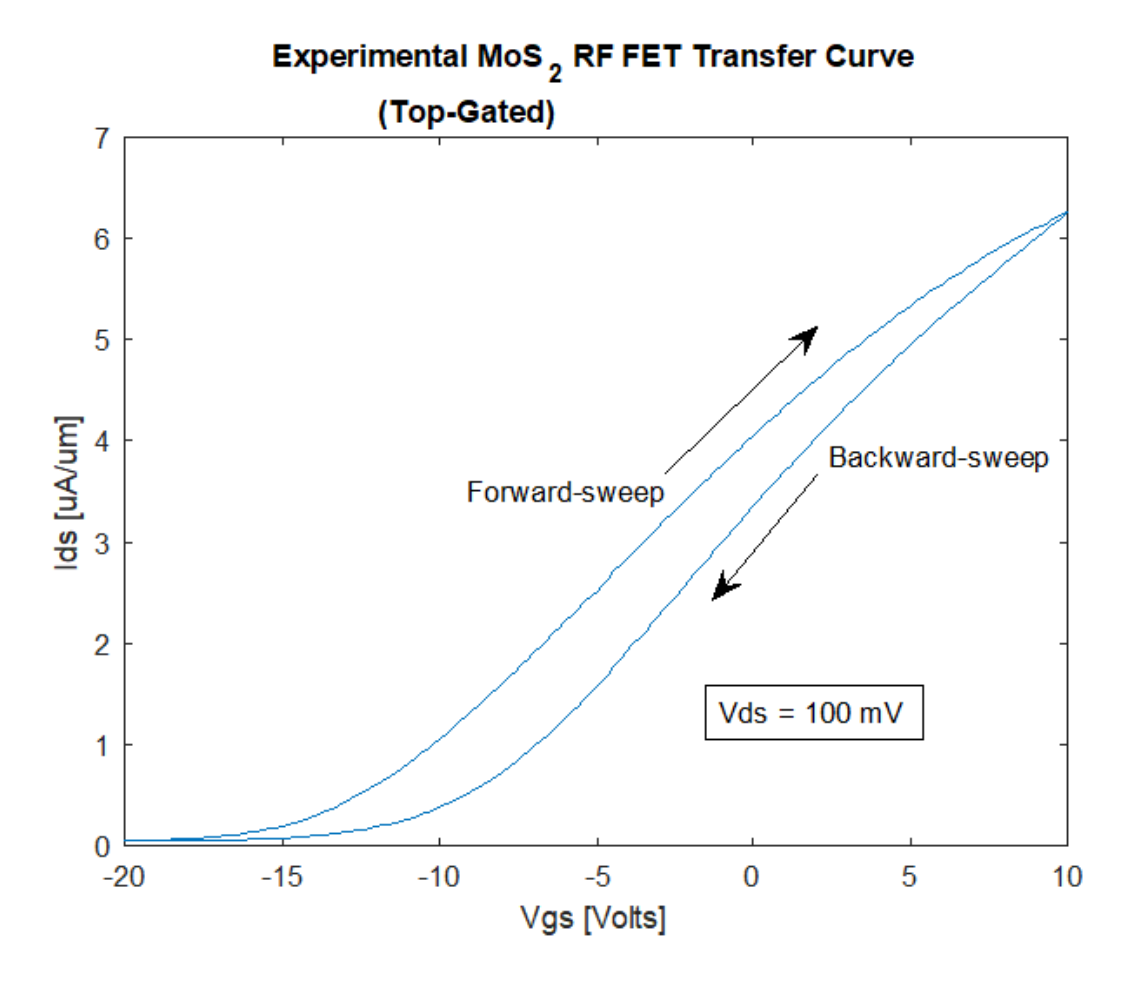


Fig. 16 Top-gated I_{DS} vs. V_{GS} example measurement

When testing the $I_{DS-}V_{DS}$ characteristics to find the location of maximum transconductance to for RF testing, saturating behavior was observed over a wide range of gate voltages (Fig. 17). These top-gated DC I-V curves will be examined in more detail in Section 3.3.

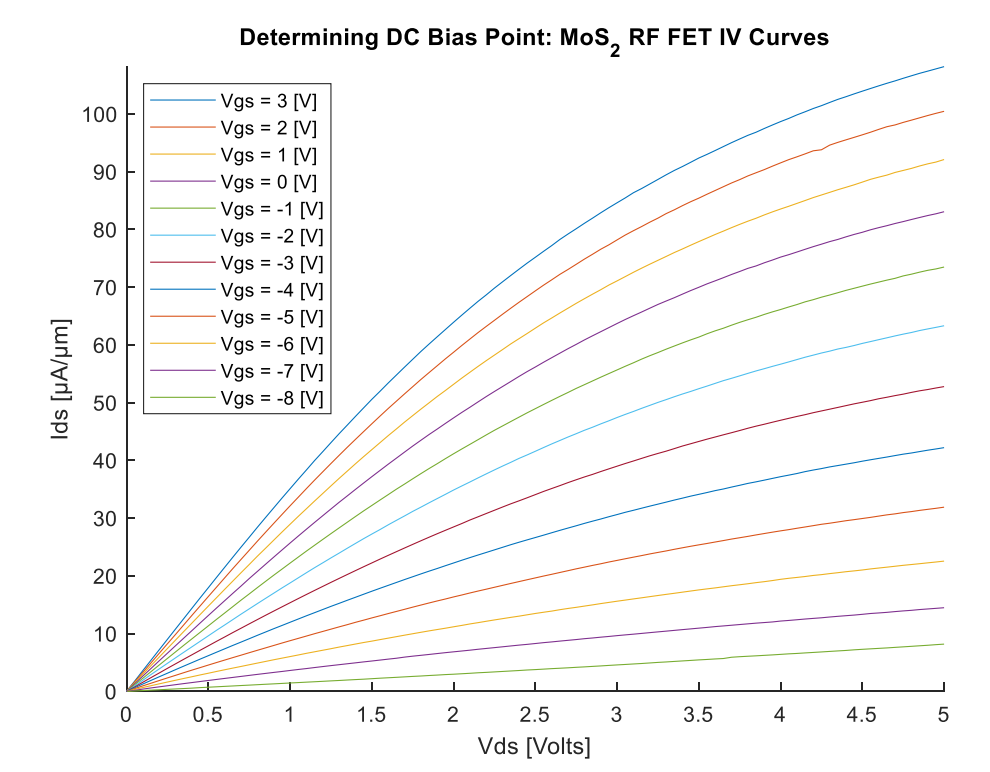


Fig. 17 Top-gated I_{DS} vs. V_{DS} example measurement

The electrical data presented in this section came from devices without the polyimide layer. In general, the devices on the polyimide substrate had a lower fabrication yield and required a higher drain bias to push a comparable current through the device.

3.2 RF Electrical Data

Common metrics to characterize RF transistors are f_T , the frequency at which there is unity current gain and f_{max} , the frequency at which there is unity power gain. These metrics were extracted from the measured S-parameters and are displayed graphically in this section by the frequency at which the curves hit 0 dB gain. These metrics can also be derived using small-signal transistor models and are often approximated as follows. 22,23

$$f_T = \frac{g_m}{2\pi(C_{gs} + C_{gd})},\tag{3}$$

$$f_{max} = \frac{f_T}{2} \sqrt{\frac{r_o}{R_g + R_i}}, \tag{4}$$

where g_m is the transconductance, C_{gs} and C_{gd} are the capacitances between the gate and the source/drain, r_o is the output resistance, R_g is the gate resistance, and R_i is the input resistance.

From the f_T metric, we calculate the saturation velocity using the formula

$$v_{sat} = 2\pi f_T L_g , \qquad (5)$$

where L_g is the gate length of 400 nm.

3.2.1 RF Performance on Rigid (SiO₂) Substrate

Results from the device with the highest measured f_T and f_{max} are plotted in Figs. 18 and 19. The device was biased with $V_{GS} = -2$ V and $V_{DS} = 5$ V.

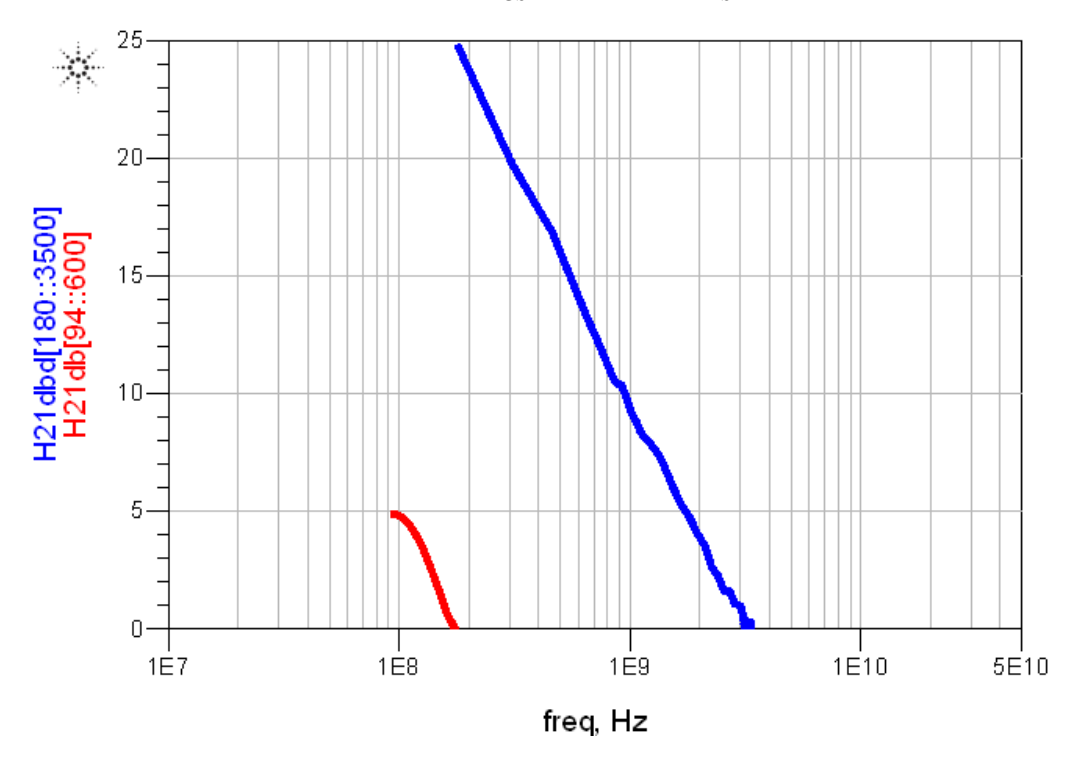


Fig. 18 Rigid substrate: $f_T \sim 180 \text{ MHz/3.3 GHz}$ (extrinsic/intrinsic)

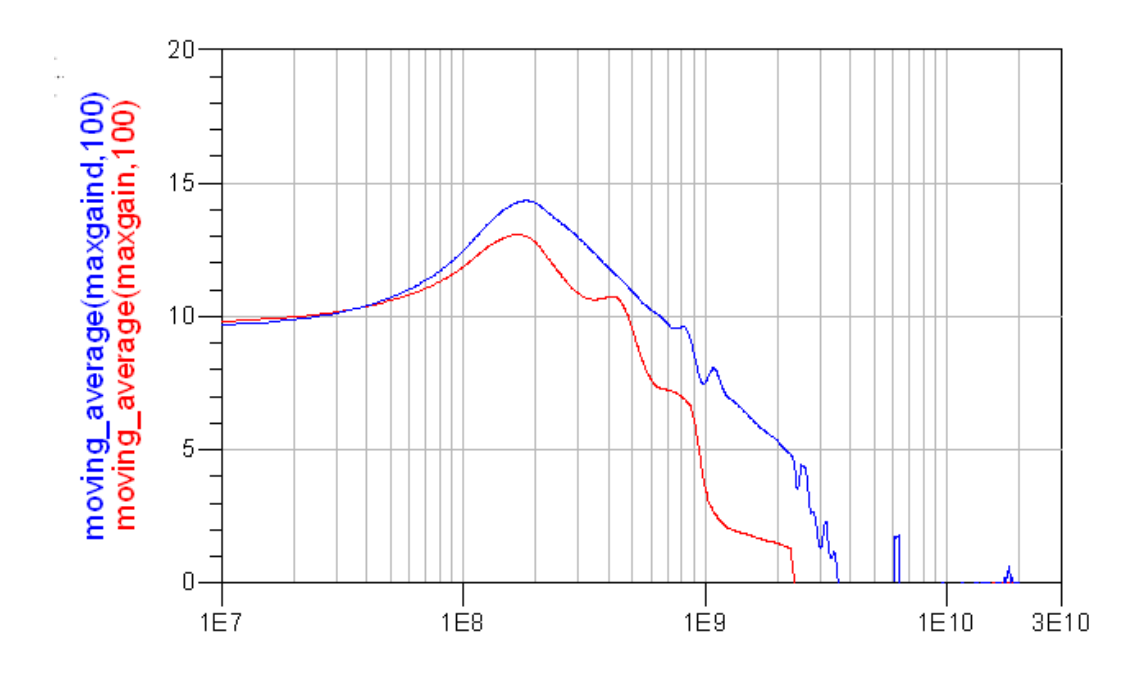


Fig. 19 Rigid substrate: $f_{max} \sim 2.4$ GHz/3.5 GHz (extrinsic/intrinsic)

3.2.2 RF Performance on Flexible (Polyimide) Substrate

Results from the device with the highest measured f_T and f_{max} are plotted in Figs. 20 and 21. The device was biased with $V_{GS} = -5$ V and $V_{DS} = 7$ V. A summary of the data is presented in Table 1.

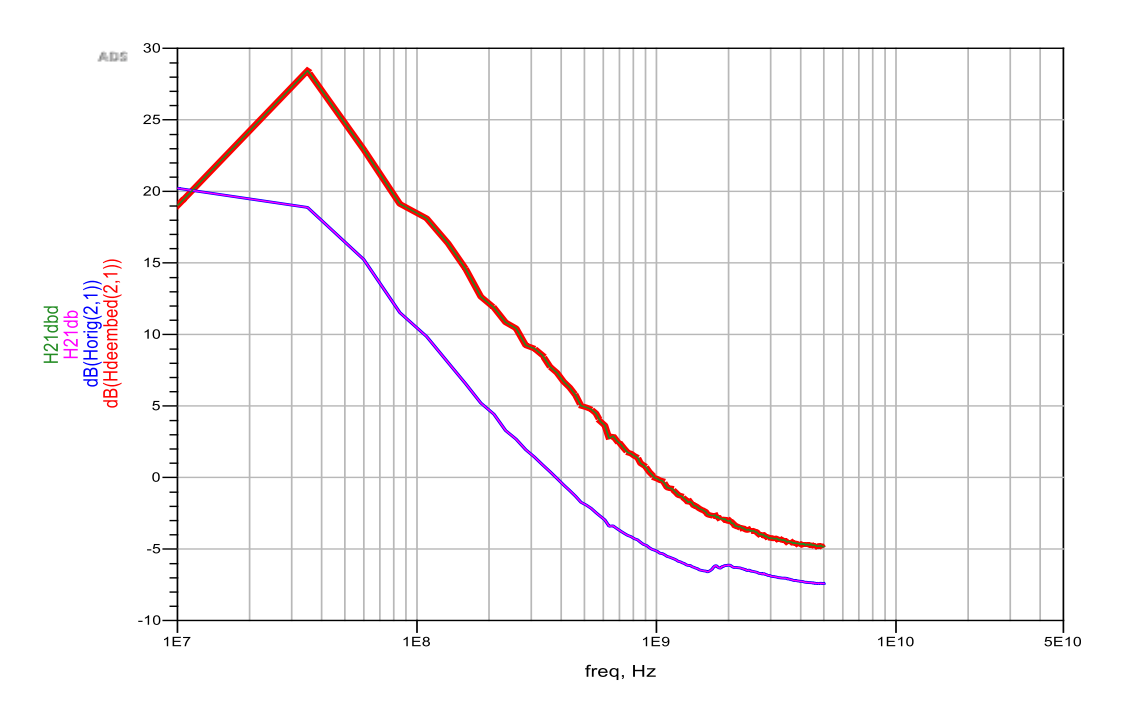


Fig. 20 Polyimide substrate: $f_T \sim 300 \text{ MHz}/1 \text{ GHz}$ (extrinsic/intrinsic)

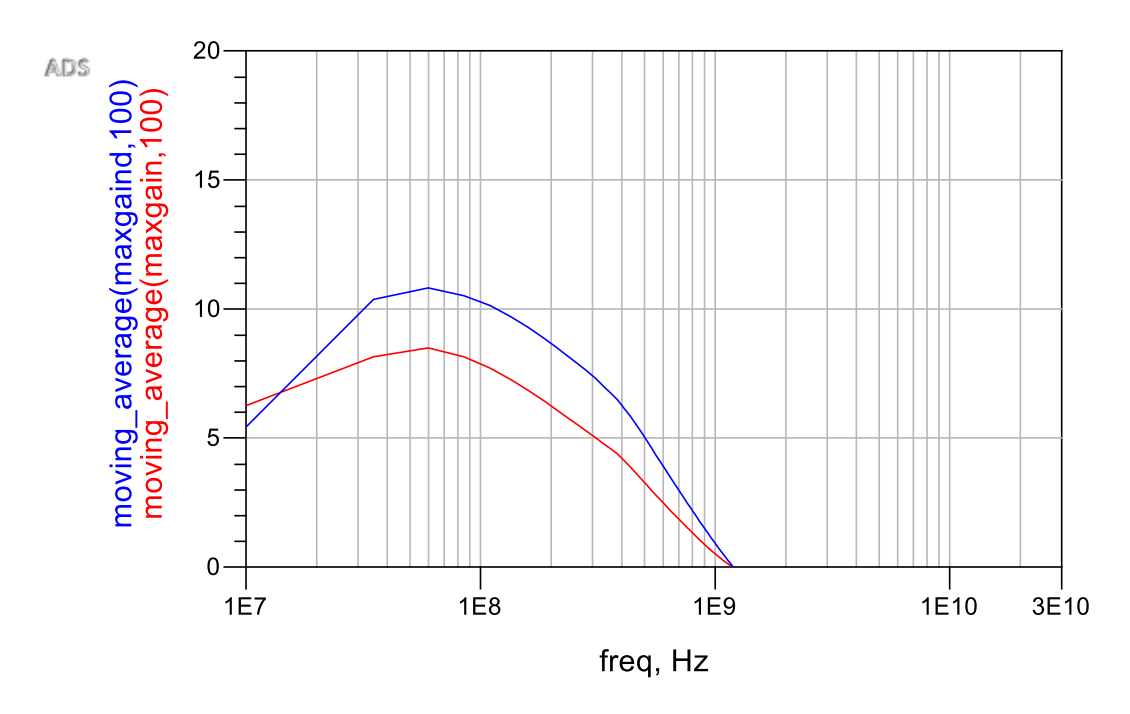


Fig. 21 Polyimide substrate: $f_{max} \sim 1.1$ GHz/1.1 GHz (extrinsic/intrinsic)

Table 1 Summary of intrinsic RF device performance

Substrate type	f _T (GHz)	f _{max} (GHz)	v _{sat} (cm/s)
Rigid (SiO ₂)	3.3	3.5	8.29×10^{5}
Flexible (polyimide)	1.0	1.1	2.51×10^{5}

3.2.3 Comparison to Monolayer RF FET Performance in Literature

For monolayer MoS₂ devices with a similar top-gated design to ours, an f_T of 6.7 GHz, f_{max} of 5.3 GHz, and v_{sat} of 1.1 × 10⁶ cm/s has been achieved with a 250-nm gate length. Using a combined metric of $f_T \cdot L_g$ to compare our devices, this device has $f_T \cdot L_g = 1.68$ GHz· μ m, whereas ours has $f_T \cdot L_g = 1.32$ GHz· μ m.

However, better performance has been achieved by switching to an embedded gate structure. With this gate-first process and a 150-nm L_g , they achieved f_T of 20 GHz, f_{max} of 11.4 GHz, and v_{sat} of 1.88 \times 10⁶ cm/s, resulting in $f_T \cdot L_g = 3.0$ GHz· μ m.

Section 3.3 of this report goes into detail calculating the mobility and contact resistance of a DEVCOM Army Research Laboratory–fabricated FET. Based on the information provided in Sanne et al. (2015, 2017), the difference in performance appears to be mainly a result of higher electron mobility.

3.2.4 RF Performance Comparison to Theoretical Limits

According to Monte Carlo simulations, the room-temperature electron velocity saturation in intrinsic MoS_2 is around 3.4×10^6 to 4.8×10^6 cm/s, although this value depends on the chosen energy separation between the K and Q valleys. This, however, only includes the intrinsic scattering from phonons originating in the MoS_2 ; other scatter processes such as from remote phonons and impurities need to be accounted for to get a more complete picture. The velocity measured in our RF FET and the embedded gate design mentioned previously are well below the theoretical phonon-limited value, though measurements of v_{sat} approaching this limit ($\sim 3.4 \times 10^6$ cm/s at room temperature) have been measured in monolayer MoS_2 FETs after accounting for device self-heating.

3.3 Device I-V Modeling

While this report focuses on devices made for RF operation, MoS₂ FETs are still a relatively new technology and investigating the DC I-V characteristics can provide useful insights. Only the top-gated devices are investigated here for modeling the I-V characteristics. The back-gated devices have extremely thick gate dielectrics (hundreds of nanometers). This thick oxide requires gate voltages up to ± 100 V to fully sweep the on/off range of the transistor. This effectively restricts operation of back-gated transistors to the linear regime since reaching the saturation condition $(V_{DS} > V_{GS} - v_{th})$ would require large drain-source biases and cause device destruction. The top-gated devices on the other hand have thin enough gate dielectrics (~25 nm) to enable saturation at feasible drain-source voltages and were tested over the range of 0–5 V V_{DS} .

3.3.1 Simple FET Model with Contact Resistance

Neglecting channel length modulation, the standard metal—oxide—semiconductor field-effect transistor (MOSFET) I-V equations are listed as follows:

Linear Regime ($V_{GS} > v_{th}$, $V_{DS} < V_{GS} - v_{th}$):

$$I_{DS LIN} = \frac{\mu_n C_{OX} W}{L} \left[[V_{GS} - V_{th}] V_{DS} - \frac{V_{DS}^2}{2} \right].$$
 (6)

Saturation Regime ($V_{GS} > v_{th}$, $V_{DS} > V_{GS} - v_{th}$):

$$I_{DS \, SAT} = \frac{\mu_n c_{OX}}{2} \frac{W}{L} [V_{GS} - V_{th}]^2 \,. \tag{7}$$

Not included in these equations is the impact of contact resistance, R_c . The main impact this has is that the applied drain-source voltage is no longer the potential

that is dropped across the channel due to some of the potential being dropped across the contact resistance. This is shown schematically in the circuit diagram provided in Fig. 22.

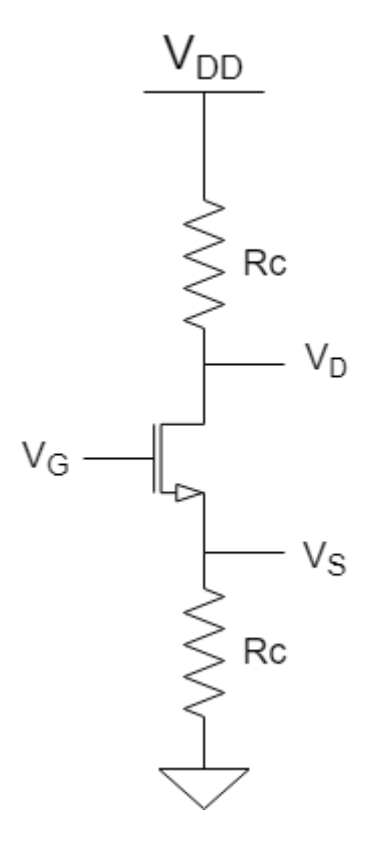


Fig. 22 Simple transistor model including contact resistances

To determine the impact that the contact resistance is having, we first assume the contact resistance does not significantly change with gate voltage since the metal contacts screen the MoS₂ underneath it from the gate electric field (unlike in the back-gated configuration where the MoS₂ under the contacts are not screened and the contact resistance is known to change significantly with gate voltage).^{19,26}

The voltage seen across the channel becomes

$$V_{DS} = V_{DD} - I_{DS} 2R_c. (8)$$

$$R_{TOTAL} = 2R_c + R_{MoS2}. (9)$$

This means the contact resistance becomes more dominant as V_{GS} increases since the resistance of the MoS₂ channel will go down as more carriers are drawn into the channel.

3.3.2 FET Model Parameter Extraction

The analysis that follows calculates contact resistance by extrapolating experimental data of R_{TOTAL} versus V_{GS} to the limit when R_{MoS2} is zero. To quantitatively see how the total resistance changes with V_{GS} , we can look at the linear regime equation and make some approximations. At low V_{DS} and higher $[V_{GS} - V_{th}]$, the quadratic term can be neglected, and linear regime equation can be approximated as linear:

$$I_{DS LIN} = \frac{\mu_n C_{OX} W}{L} [V_{GS} - V_{th}] V_{DS}. \tag{10}$$

This enables straightforward calculation of the resistance of the MoS₂ channel:

$$R_{MoS2} = \frac{V_{DS}}{I_{DS\,LIN}} = \frac{L}{\mu_n C_{OX} W[V_{GS} - V_{th}]}.$$
 (11)

Figure 23 shows experimental $I_{DS} - V_{DS}$ curves obtained from testing a MoS₂ RF FET over a wide range of gate voltages. The total resistance was determined experimentally via Ohm's law for each gate voltage in the region highlighted by the green box ($V_{DS} < 0.6 \text{ V}$).

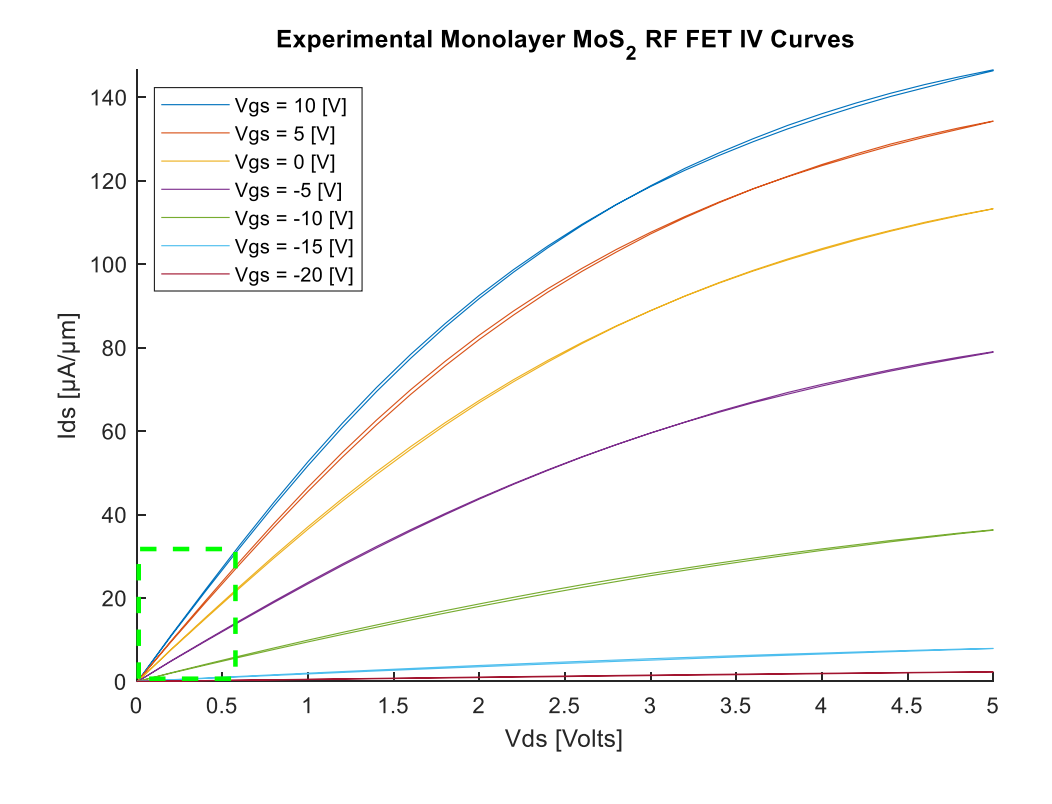


Fig. 23 $I_{DS-}V_{DS}$ curve of an RF FET on the rigid substrate. Dashed green box indicates region used to fit FET parameters.

 R_{TOTAL} was fitted numerically as a function of V_{GS} in MATLAB with three unknowns:

$$R_{TOTAL} = X_1 + \frac{X_2}{(V_{GS} - X_3)},$$
 (12)

where $X_1 = 2R_c$, $X_2 = \frac{L}{\mu_n C_{OX}W}$, and $X_3 = V_{th}$. This fitting enabled simultaneous determination of the contact resistance, threshold voltage, and the product of the mobility and gate capacitance. Looking at how well the function fits the raw data, we can determine if our inherent assumptions (such as contact resistance and mobility not depending heavily on V_{GS}) are valid.

Figure 24 shows the fitting of experimental data with the model, demonstrating the high degree of accuracy, meaning either our assumptions were correct or that they happen to offset each other.

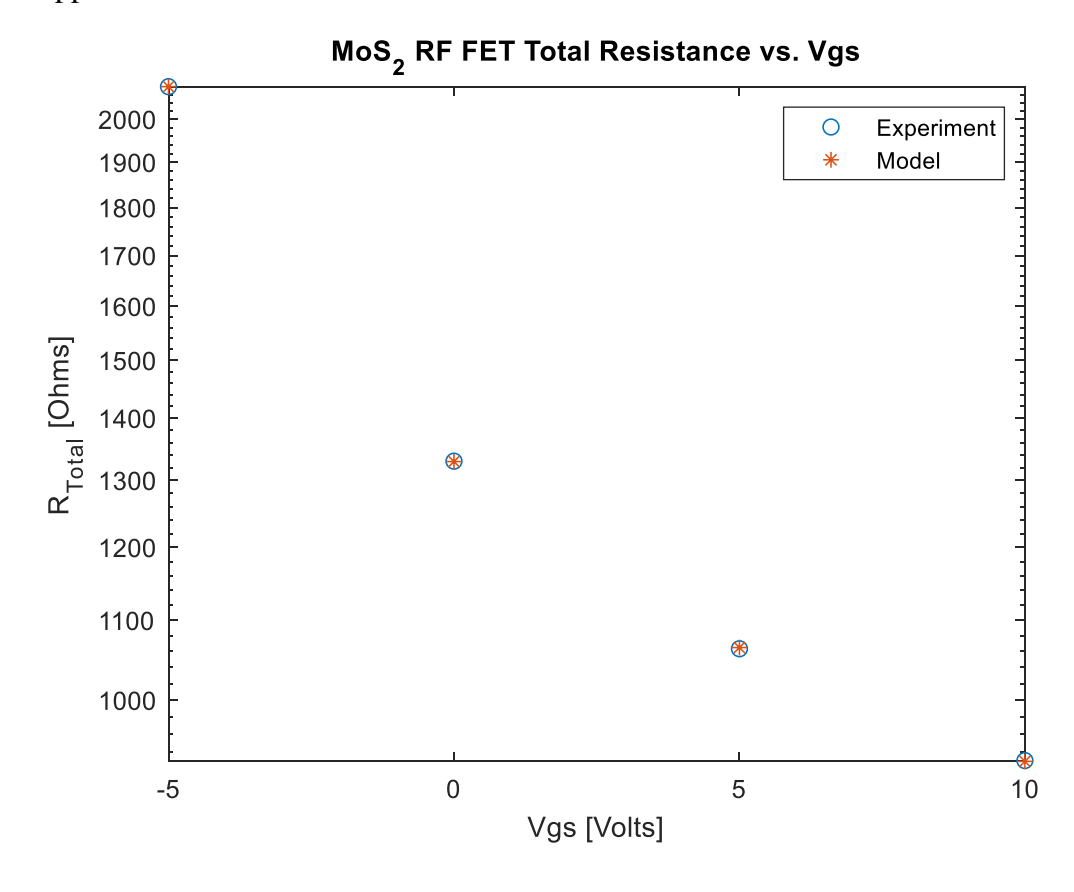


Fig. 24 Total resistance: experimental values compared to the model

The extracted fitting parameters were $X_1 = 2R_c = 512 \,\Omega$ (2.56 k $\Omega \cdot \mu$ m), $X_2 = \frac{L}{\mu_n C_{OX} W} = 8542.6 \,V^2/A$, and $X_3 = V_{th} = -10.45 \,V$. Using W = 20 μ m, L = 400 nm, and the top-gated parameters listed in Section 2.5, $\mu_n = 7.345 \,\mathrm{cm}^2/\mathrm{V} \cdot \mathrm{s}$.

Figure 25 shows an extrapolation of the model to a wider range of gate voltages and the extracted limit of $2R_c$, as well as the calculated threshold voltage.

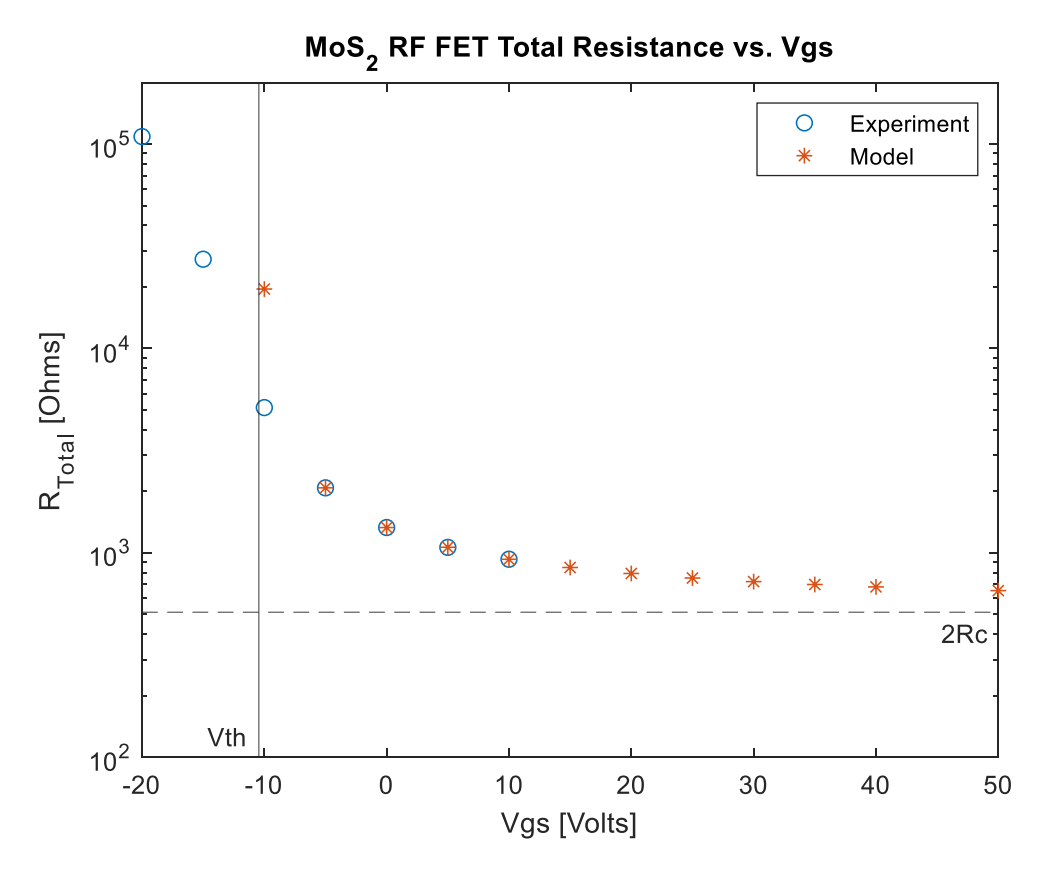


Fig. 25 Extrapolation of the total resistance to higher gate voltages, showing the limit of twice the contact resistance as the dashed horizontal line and threshold voltage as the vertical line

3.3.3 Parameter Validation and Low-Field Mobility Calculation

The threshold voltage calculated with this model (-10.45 V) agrees with the qualitative behavior of the RF FET's $I_{DS} - V_{GS}$ curve (Fig. 26).

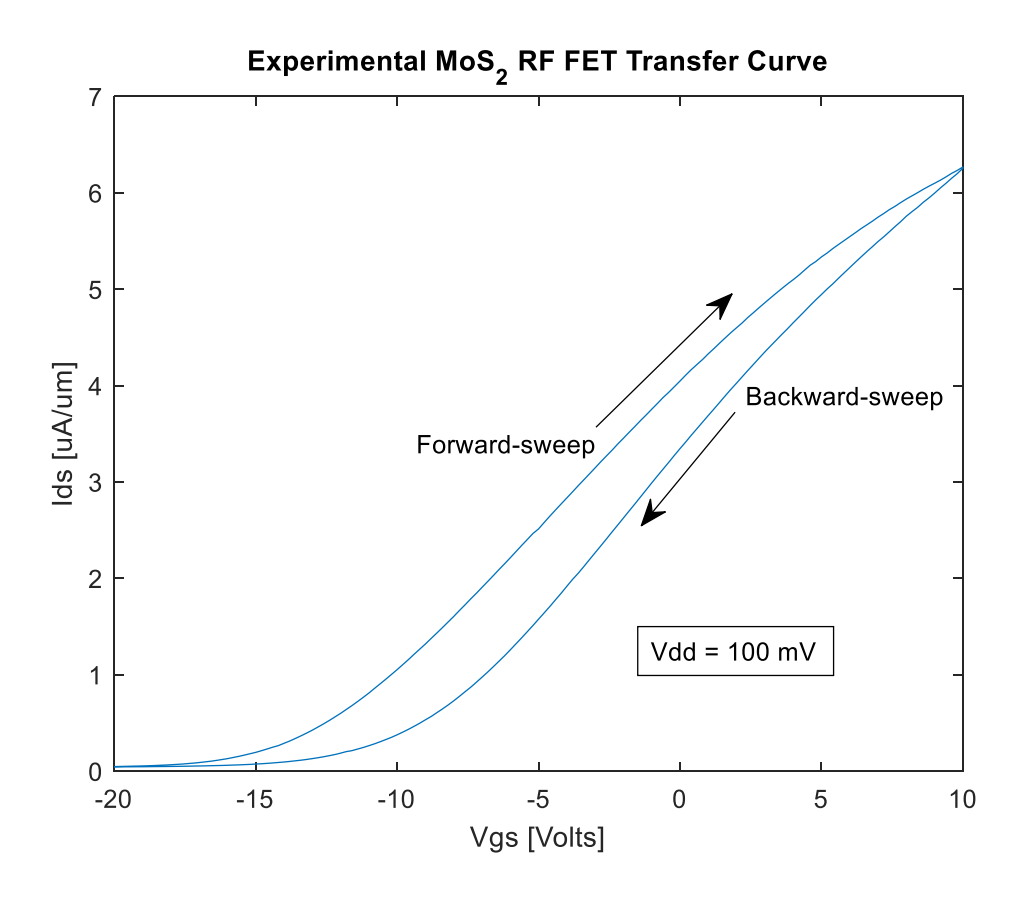


Fig. 26 RF FET $I_{DS-}V_{GS}$ curve (notice the extracted threshold voltage of -10.45 from the $I_{DS-}V_{DS}$ curves qualitatively makes sense)

After determining R_c , we calculate the voltage dropping across the contacts $(2R_cI_{DS})$ versus the voltage dropping across the channel $(V_{DD} - 2R_cI_{DS})$ (Fig. 27).

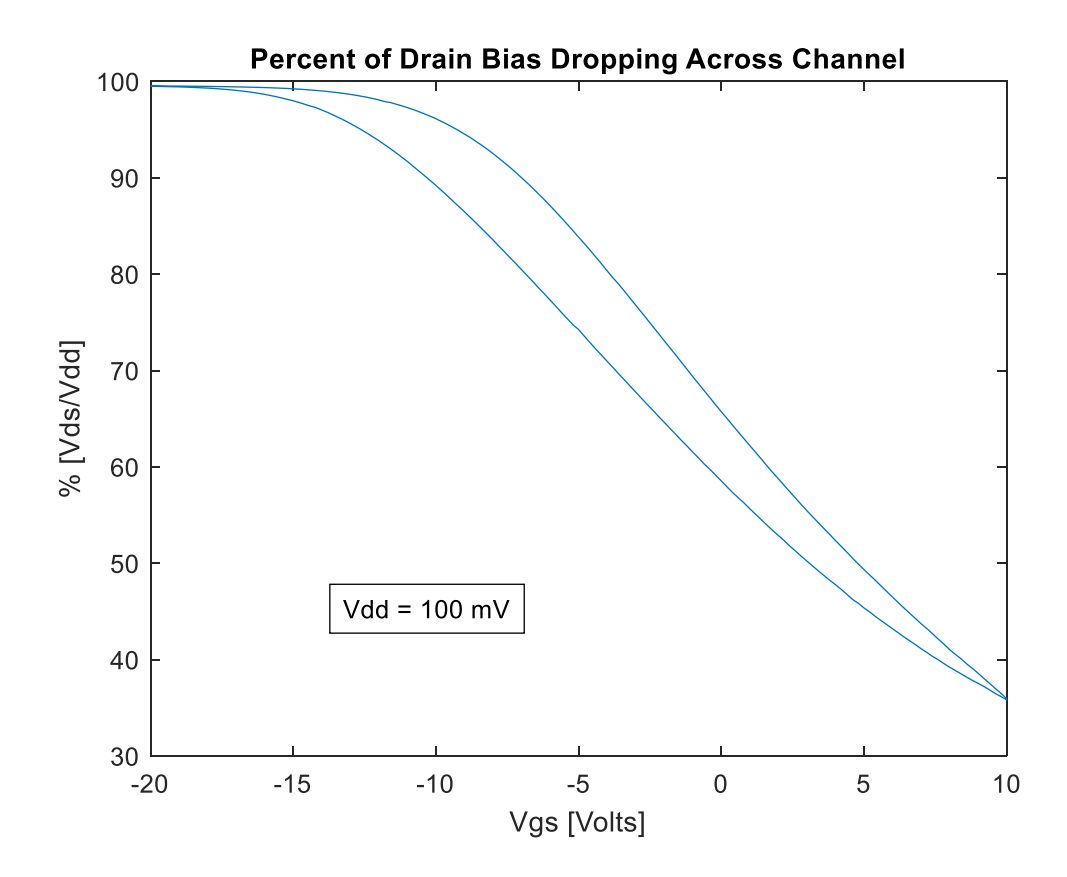


Fig. 27 After extracting the contact resistance, we can determine how much of the applied voltage V_{DD} is dropped across the channel vs. the contact resistance. At low gate voltages most of the voltage drops across the channel, but at high gate voltages most drops across the contact resistance.

Based on this result, once the gate voltage is 5 V or higher, most of the applied voltage is dropping across the parasitic contact resistance rather than the MoS_2 channel.

Next we looked at how the contact resistance impacts the extraction of the field-effect mobility from the transfer curve. As mentioned earlier, mobility is normally calculated from the I_{DS} – V_{GS} curve with the following formula:

$$\mu_{FE} = \frac{d\frac{I_{DS}}{v_{DS}}}{dv_{GS}} \frac{L}{c_{OX}W}.$$
 (13)

Without considering the impact of contact resistance, the V_{DS} term is considered to be the same as the applied voltage V_{DD} . Figure 28 shows the extraction of mobility from the transfer curve without including contact resistance.

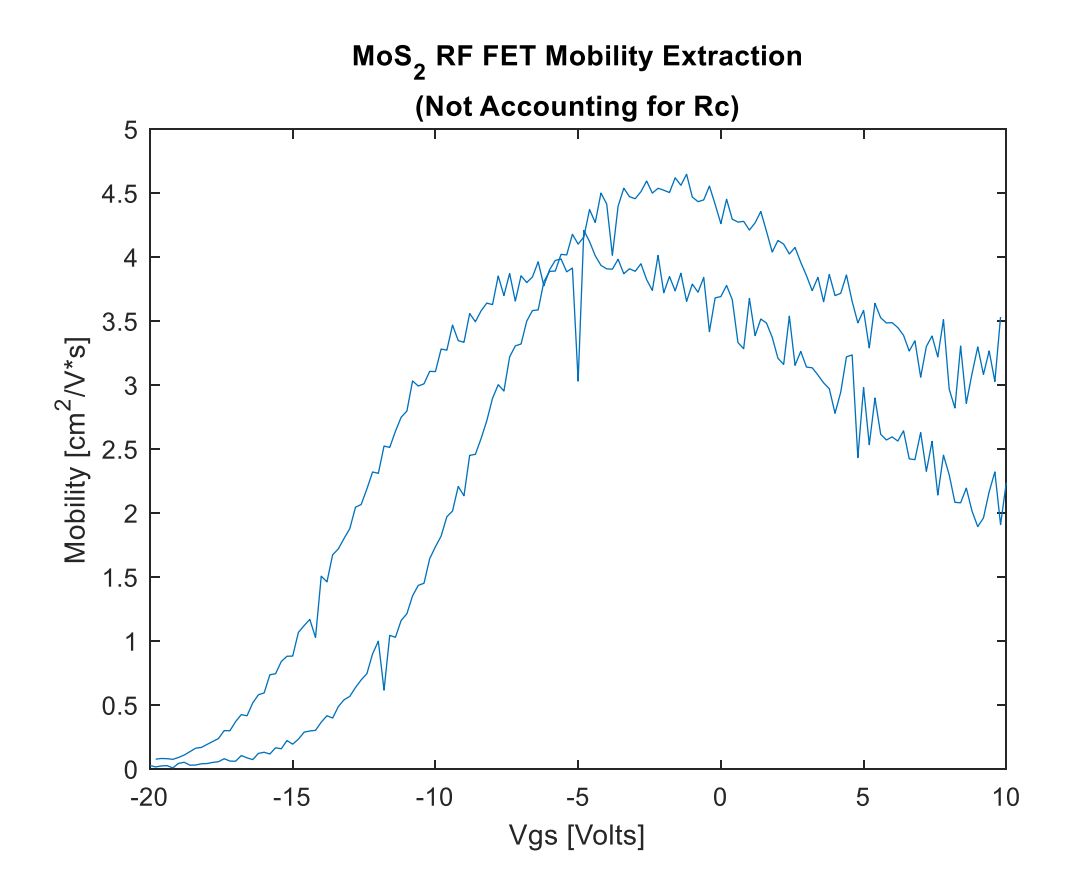


Fig. 28 Field-effect mobility extracted from the RF FET $I_{DS-}V_{GS}$ curve as measured (not considering contact resistance)

When including the impact of contact resistance, the V_{DS} term is equal to $V_{DD} - I_{DS} 2R_C$. Figure 29 shows the extraction of mobility from the transfer curve while including contact resistance and averaging the two sweep directions. Note that extracted field-effect mobility approaches the 7.345 cm²/V·s value determined by the total resistance model.

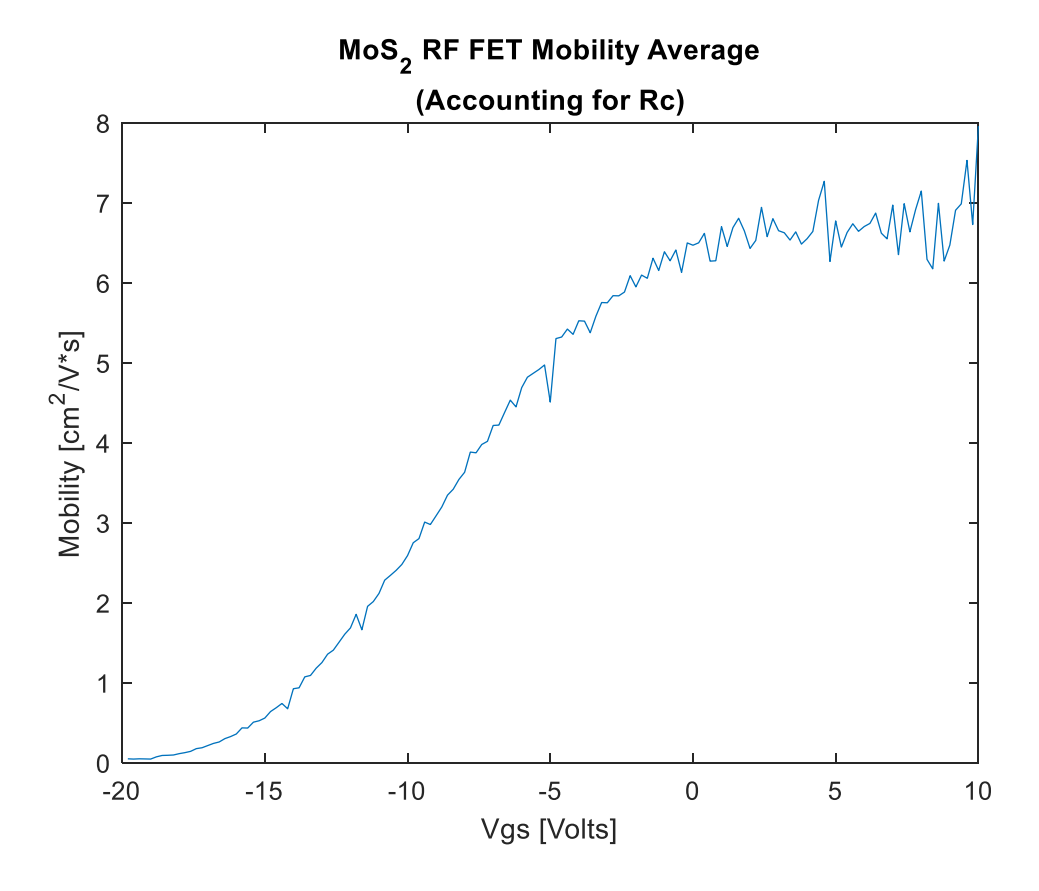


Fig. 29 Field-effect mobility extracted from the RF FET $I_{DS-}V_{GS}$ curve after incorporating the voltage dropped across the contact resistance

3.3.4 FET Model Inaccuracies at High Gate and Drain Fields

After extracting values for electron mobility, contact resistance, and threshold voltage from the low V_{DS} region of operation, we applied these parameters to the whole range of V_{GS} and V_{DS} to determine the accuracy of the simple transistor equations and where the model breaks down.

Looking at the experimental I_{DS} – V_{DS} data (Fig. 23), and knowing that the threshold voltage is -10.45 V, clearly the device does not follow the transistor equations at high gate biases. Since V_{DD} is 5 V and the threshold voltage is -10.45 V, the device should be in the linear regime for $V_{GS} > 0$ V as the saturation condition would not be reached. Additionally, the spacing between the lines at $V_{DS} = 5$ V should be linear between the gate voltages; however, the spacing clearly is sublinear.

We know that the contact resistance plays an important role in the device performance and that a significant portion of the applied potential drops across the contact resistance instead of the channel. Therefore, the first goal is to determine how the contact affects the I_{DS} – V_{DS} curves.

We first compute and plot the entire range of I_{DS} – V_{DS} curves using the extracted parameters and not including contact resistance (Fig. 30).

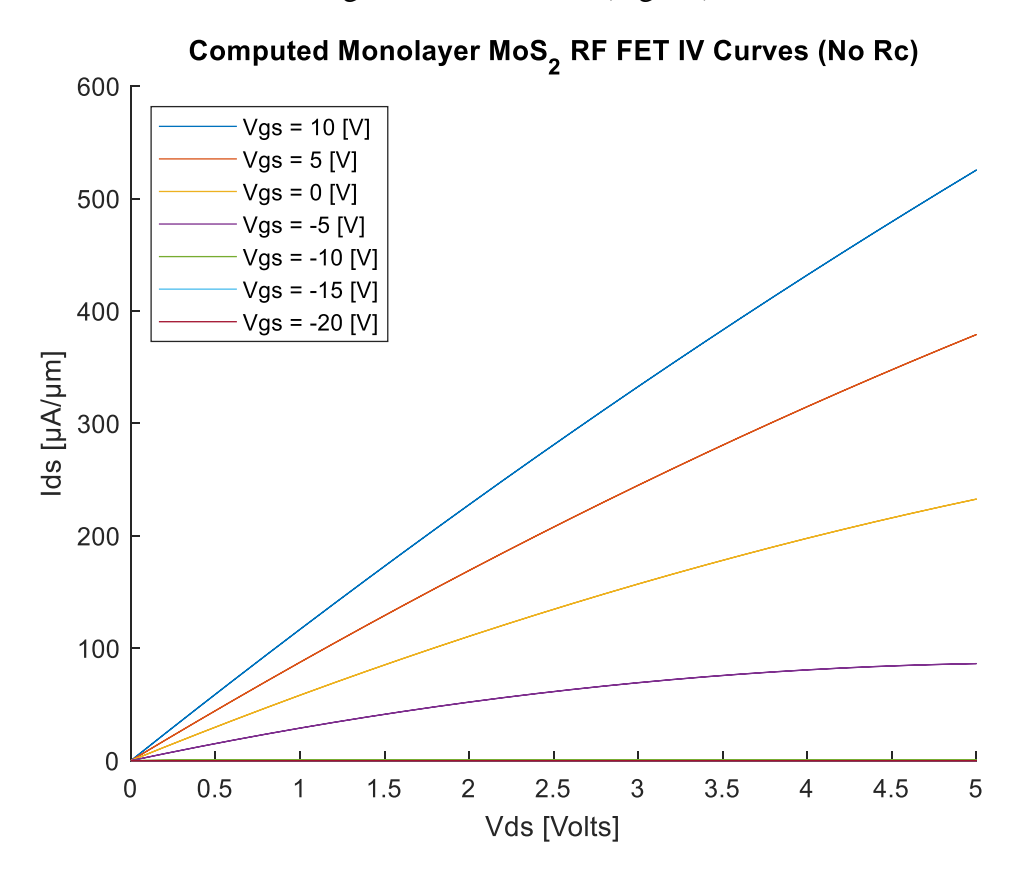


Fig. 30 $I_{DS-}V_{DS}$ curves plotted using extracted values X2 and X3

Next, as before, the voltage drop across the contact resistance is calculated as $I_{DS}2R_C$ (Fig. 31).

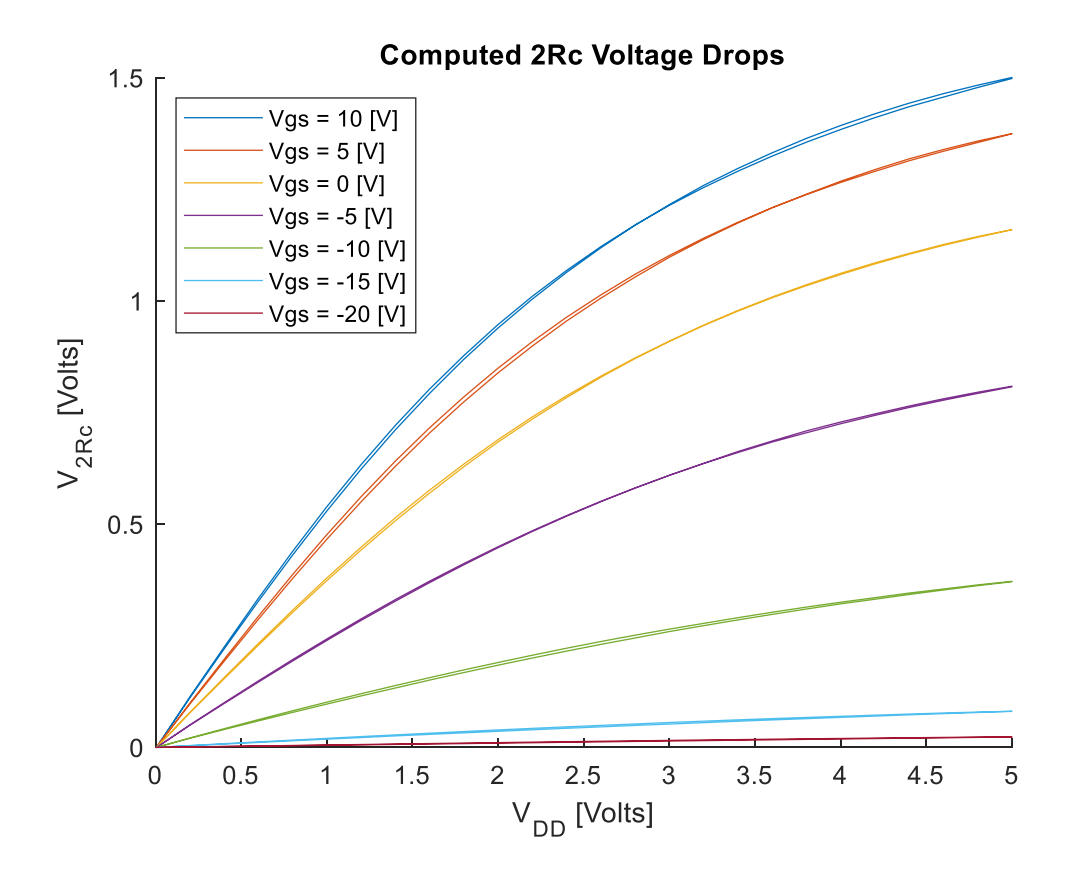


Fig. 31 Calculated voltage drops due to contact resistance, X1. The specific contact resistance of this device was 2.56 k Ω · μ m.

Next, we include the impact of contact resistance by updating the V_{DS} term and plotting against V_{DD} instead (Fig. 32).

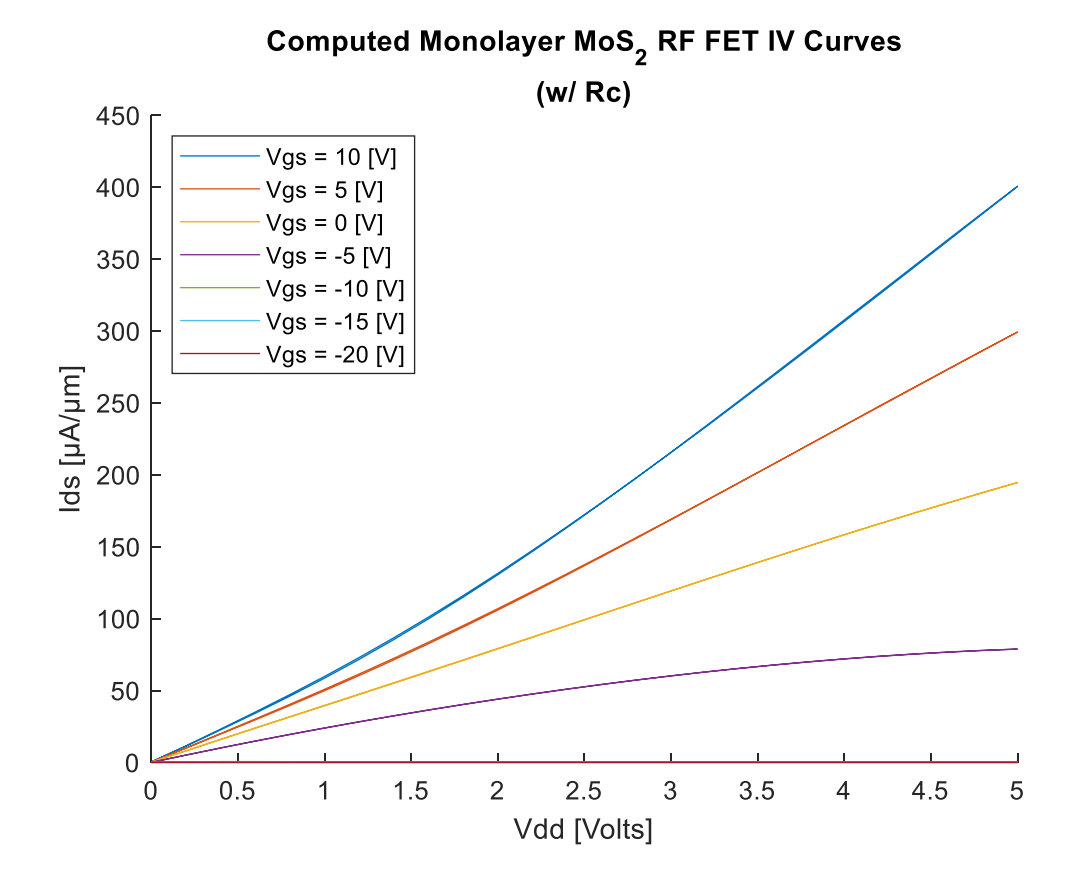


Fig. 32 I_{DS}-V_{DD} curves plotted using extracted values X1, X2, and X3

Next, the computed $I_{DS-}V_{DD}$ curves are plotted alongside the experimental $I_{DS-}V_{DD}$ curves to determine where the model is no longer accurate (Fig. 33).

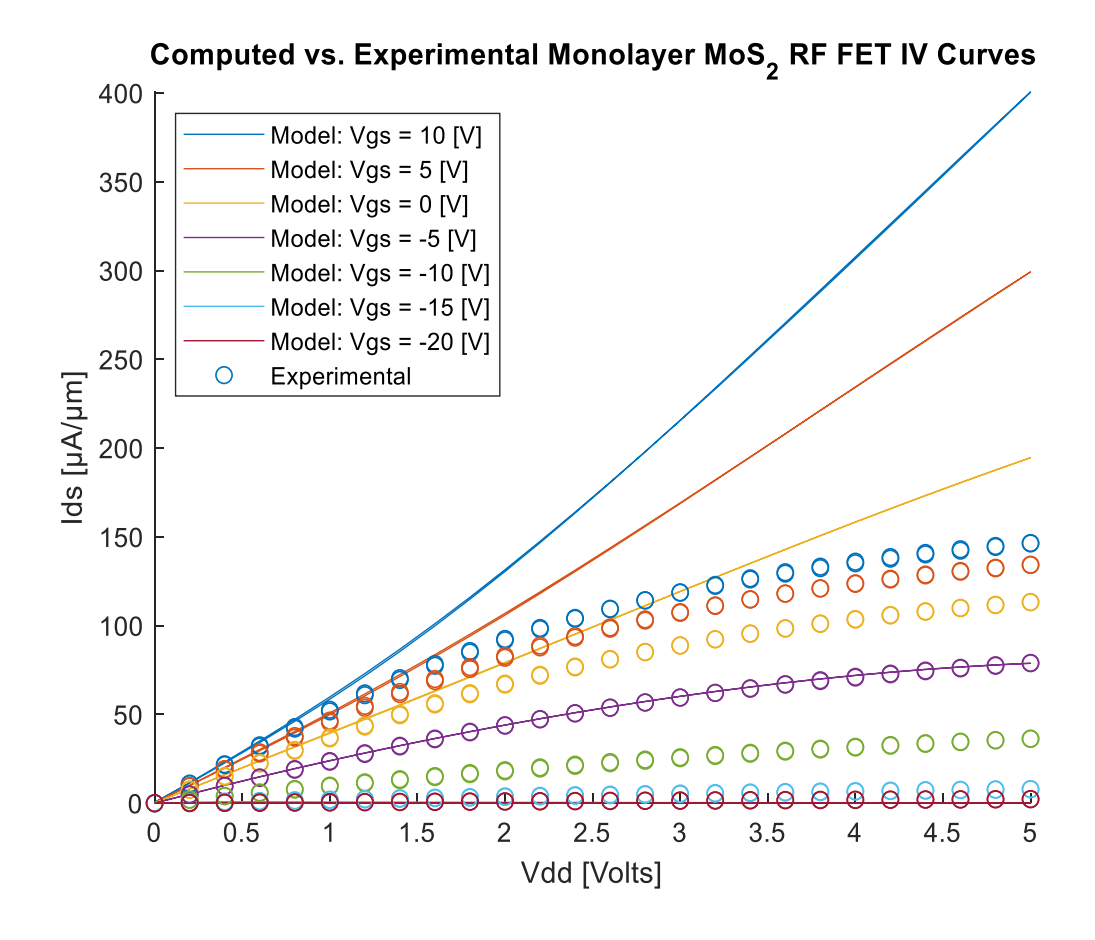


Fig. 33 Experimental results vs. computed $I_{DS-V_{DD}}$ curves plotted using extracted values X1, X2, and X3

It is worth noting that for smaller gate overdrives ($V_{GS} = -5$ V), the transistor equations describe the experimental data well after including contact resistance. However, clearly incorporating the impact of contact resistance alone does not accurately recreate the experimental device performance in the regions where there is both a high gate and drain bias. Other groups have noticed this behavior as well, and often attribute it to "velocity saturation". In the work by Smithe et al., they determine that significant heating occurs at high drain and gate biases.²⁵

Zooming in to look at the low drain-bias region (V_{DD} < 2 V), we can see the model is indeed more accurate at lower biasing (Fig. 34).

Computed vs. Experimental Monolayer MoS₂ RF FET IV Curves

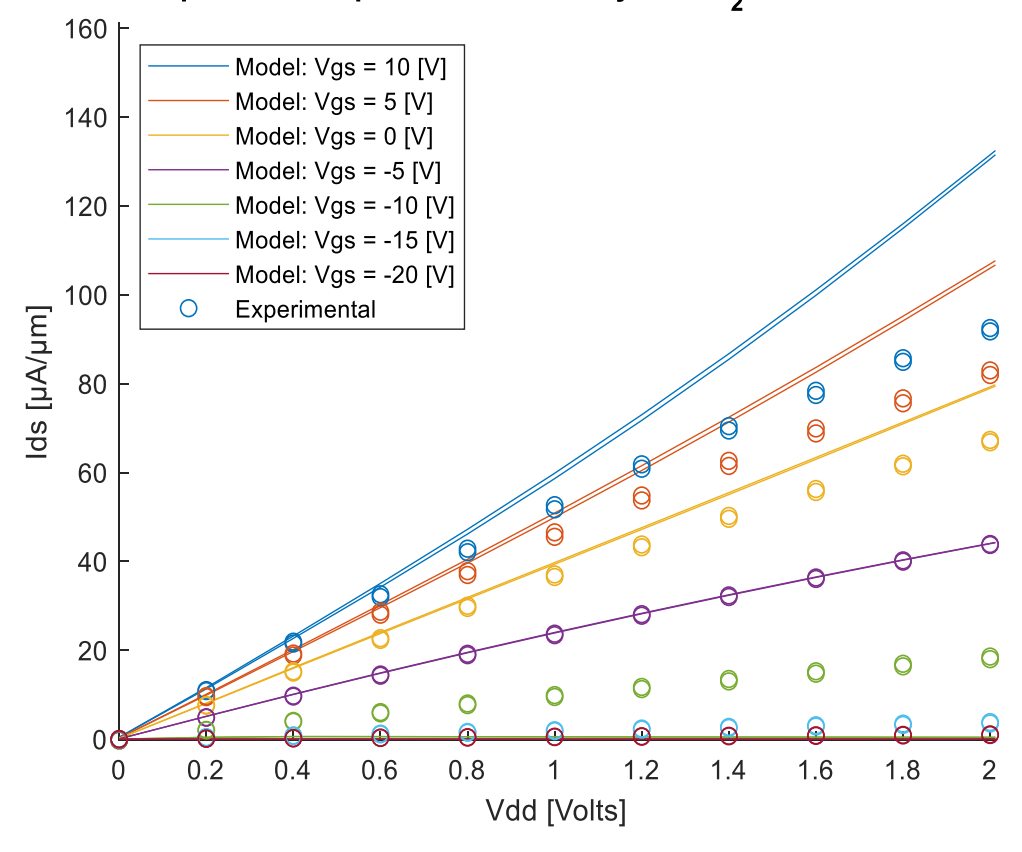


Fig. 34 Experimental results vs. computed I_{DS} - V_{DD} curves plotted using extracted values X1, X2, and X3. Subthreshold current modeling was ignored for simplicity; this explains the low current computed for $V_{GS} < -10$ V.

4. Conclusions

RF FETs using ARL-grown, monolayer MoS₂ as the semiconducting channel were fabricated and tested in the GSG configuration. Devices were fabricated and characterized on both hard (SiO₂) and flexible (polyimide) substrates. Devices operated with de-embedded f_T and f_{max} over 3 GHz on rigid substrates and 1 GHz on flexible substrates. The performance of the devices was compared to other monolayer MoS₂ RF FET performance published in literature^{13,14} and to the theoretical maximum performance of phonon-limited transport. Standard MOSFET current-voltage equations were applied to experimental results of ARL-fabricated RF transistors. A method to accurately extract the key device parameters of threshold voltage, contact resistance, and transconductance was introduced and discussed. The experimental transistor current-voltage curves deviate from the transistor models in regions of operation with both a high gate and drain bias. According to related literature, device self-heating occurs at these operation regimes causing significant velocity saturation and mobility degradation.

5. References

- 1. Novoselov KS, Geim AK, Morozov SV, Jiang D, Zhang Y, Dubonos SV, Grigorieva IV, Firsov AA. Electric field effect in atomically thin carbon films. Science. 2004;306(5696):666–669. doi:10.1126/science.1102896.
- 2. Novoselov KS, Jiang D, Schedin F, Booth TJ, Khotkevich VV, Morozov SV, Geim AK. Two-dimensional atomic crystals. Proc Natl Acad Sci USA. 2005;102(30):10451–10453. doi:10.1073/pnas.0502848102.
- 3. Mak KF, Lee C, Hone J, Shan J, Heinz TF. Atomically thin MoS₂: a new direct-gap semiconductor. Phys Rev Lett. 2010;105:136805.
- 4. Splendiani A, Sun L, Zhang Y, Li T, Kim J, Chim CY, Galli G, Wang F. Emerging photoluminescence in monolayer MoS₂. Nano Lett. 2010;10(4):1271–1275. doi:10.1021/nl903868w.
- 5. Radisavljevic B, Radenovic A, Brivio J, Giacometti V, Kis A. Single-layer MoS₂ transistors. Nat Nanotechnol. 2011;6(3):147–150. doi:10.1038/nnano.2010.279.
- 6. Fuhrer MS, Hone J. Measurement of mobility in dual-gated MoS₂ transistors. Nat Nanotechnol. 2013;8:146–147. doi:10.1038/nnano.2013.30.
- 7. Lee YH, Zhang XQ, Zhang W, Chang MT, Lin CT, Chang KD, Yu YC, Wang JT, Chang CS, Li LJ, Lin TW. Synthesis of large-area MoS₂ atomic layers with chemical vapor deposition. Adv Mater. 2012;24(17):2320–2325. doi:10.1002/adma.201104798.
- 8. Schwierz F. Graphene transistors: status, prospects, and problems. Proc IEEE 101. 2013:1567–1584.
- 9. Schwierz F. Performance of graphene and beyond graphene 2-D semiconductor devices. Invited paper. ECS Trans. 2015;69(10):231–240.
- 10. Akinwande D, Petrone N, Hone J. Two-dimensional flexible nanoelectronics. Nat Commun. 2014;5:5678.
- 11. Ayari A, Cobas E, Ogundadegbe O, Fuhrer MS. Realization and electrical characterization of ultrathin crystals of layered transition-metal dichalcogenides. J Appl Phys. 2007;101:014507.

- 12. US Army Research Laboratory. Army Research Laboratory biennial performance plan FY 16/17. 2015 Dec. https://arl.apgea.army.mil/intranet/odir/ARLAnnualPerfPlans_Rpts/FY16-17%20ARL%20Biennial%20Performance%20Plan.pdf. p. 81–82.
- 13. Sanne A, Ghosh R, Rai A, Yogeesh MN, Shin SH, Sharma A, Jarvis K, Mathew L, Rao R, Akinwande D, et al. Radio frequency transistors and circuits based on CVD MoS₂. Nano Lett. 2015;15(8):5039–5045. doi:10.1021/acs.nanolett.5b01080.
- 14. Sanne A, Park S, Ghosh R, Yogeesh MN, Liu C, Mathew L, Rao R, Akinwande D, Banerjee SK. Embedded gate CVD MoS₂ microwave FETs. npj 2-D Mater Appl. 2017;1:26. doi:10.1038/s41699-017-0029-z.
- 15. Jin Z, Li X, Mullen JT, Kim KW. Intrinsic transport properties of electrons and holes in monolayer transition-metal dichalcogenides. Phys Rev B. 2014;90(4):045422. doi:10.1103/PhysRevB.90.045422.
- 16. Li X, Mullen JT, Jin Z, Borysenko KM, Nardelli MB, Kim KW. Intrinsic electrical transport properties of monolayer silicene and MoS₂ from first principles. Phys Rev B. 2013;87:115418. doi:10.1103/PhysRevB.87.115418.
- 17. Chipara AC, Mazzoni AL, Burke RA, Nichols BM, Chin ML, Najmaei S, Zakar E, Dubey M. Process development for reactive-ion etching of molybdenum (MoS₂) utilizing a poly(methyl methacrylate) (PMMA) etch mask. Army Research Laboratory (US); 2017 Oct. Report No: ARL-TR-8192.
- 18. Koolen MCAM, Geelen JAM, Versleijen MPJG. An improved de-embedding technique for on-wafer high-frequency characterization. In: Jopke J, editor. Proceedings of the 1991 Bipolar Circuits and Technology Meeting; 1991 Sep 9–10; Minneapolis, MN; IEEE; p. 188–191. doi:10.1109/BIPOL.160985.
- Mazzoni AL, Burke RA, Chin ML, Hwee MJ. Effects of growth conditions on the measured electrical properties of monolayer molybdenum disulfide. Army Research Laboratory (US); 2017 Feb. Report No.: ARL-TR-7949.
- 20. Na J, Joo MK, Shin M, Huh J, Kim JS, Piao M, Jin JE, Jang HK, Choi HJ, Shim JH, Kim GT. Low-frequency noise in multilayer MoS₂ field-effect transistors: the effect of high-k passivation. Nanoscale. 2014;6(1):433–441. doi:10.1039/c3nr04218a.
- Mazzoni A, Chin M, Burke R, Price K, Valentin M, Najmaei S. Monolayer molybdenum disulfide common-source amplifiers on rigid and flexible substrates. Army Research Laboratory (US); 2019 July. Report No.: ARL-TR-8742.

- 22. Tasker PJ, Hughes B. Importance of source and drain resistance to the maximum $f/_T$ of millimeter-wave MODFETs. IEEE Electron Device Lett. 1989;10(7):291–293. doi:10.1109/55.29656.
- 23. Wang H, Wang X, Xia F, Wang L, Jiang H, Xia Q, Chin ML, Dubey M, Han S-j. Black phosphorus radio-frequency transistors. Nano Lett. 2014;14(11):6424–6429. doi:10.1021/nl5029717.
- 24. Zeng L, Xin Z, Chen S, Du G, Kang J, Liu X. Remote phonon and impurity screening effect of substrate and gate dielectric on electron dynamics in single layer MoS₂. Appl Phys Lett. 2013;103(11):113505. doi:10.1063/1.4821344.
- 25. Smithe KKH, English CD, Suryavanshi SV, Pop E. High-field transport and velocity saturation in synthetic monolayer MoS₂. Nano Lett. 2018;18(7):4516–4522. doi:10.1021/acs.nanolett.8b01692.
- 26. Liu W, Sarkar D, Kang J, Cao W, Banerjee K. Impact of contact on the operation and performance of back-gated monolayer MoS₂ field-effect-transistors. ACS Nano. 2015;9(8):7904–7912. doi:10.1021/nn506512j.

List of Symbols, Abbreviations, and Acronyms

2-D two-dimensional

Ag silver

Al aluminum

Al₂O₃ aluminum oxide

ARL Army Research Laboratory

Au gold

CAD computer-aided design

CF₄ tetrafluoromethane

Cl₂ chlorine gas

CVD chemical vapor deposition

DC direct current

DEVCOM US Army Combat Capabilities Development Command

DI deionized

EBL electron beam lithography

FET field-effect transistor

GSG ground-signal-ground

I_{DS} drain-source current

I-V current-voltage

IPA isopropyl alcohol (isopropanol)

KOH potassium hydroxide

MIBK methyl isobutyl ketone

MoO₃ molybdenum trioxide

MoS₂ molybdenum disulfide

MOSFET metal-oxide-semiconductor field-effect transistor

N₂ nitrogen

Ni nickel

 O_2 oxygen

PEALD plasma-enhanced atomic layer deposition

PEDOT:PSS poly(3,4-ethylenedioxythiophene)-poly(styrenesulfonate)

PMMA polymethyl methacrylate

RF radio frequency

RIE reactive ion etching

rpm revolutions per minute

Si silicon

SiO₂ silicon dioxide

Ti titanium

TMA trimethylaluminum

V volts

V_{DS} drain-source voltage

V_{GS} gate-source voltage

- 1 DEFENSE TECHNICAL
- (PDF) INFORMATION CTR DTIC OCA
 - 1 DEVCOM ARL
- (PDF) FCDD RLD DCI TECH LIB
- 11 DEVCOM ARL
- (PDF) FCDD RLS G

R BURKE

FCDD RLS EE

M CHIN

M DUBEY

S NAJMAEI

FCDD RLS EM

J PULSKAMP

A MAZZONI

C MORRIS

FCDD RLS ER

K KINGKEO

P SHAH

G BIRDWELL

T IVANOV